

Supplemental document accompanying submission to *Optica*

**Title:** pixOL: pixel-wise dipole-spread function engineering for simultaneously measuring the 3D orientation and 3D localization of dipole-like emitters

**Authors:** Matthew Lew, Tingting Wu, Jin Lu

**Submitted:** 12/20/2021 5:42:56 PM

OPTICA  
PUBLISHING GROUP  
Formerly OSA

# Dipole-spread function engineering for simultaneously measuring the 3D orientations and 3D positions of fluorescent molecules: supplementary material

TINGTING WU<sup>1,2</sup>, JIN LU<sup>1,2</sup>, AND MATTHEW D. LEW<sup>1,2,3,\*</sup>

<sup>1</sup>Department of Electrical and Systems Engineering, Washington University in St. Louis, Missouri 63130, USA

<sup>2</sup>Center for Science and Engineering of Living Systems, Washington University in St. Louis, Missouri 63130, USA

<sup>3</sup>Institute of Materials Science and Engineering, Washington University in St. Louis, Missouri 63130, USA

\*Corresponding author: mdlew@wustl.edu

---

This document provides supplementary information for “Dipole-spread function engineering for simultaneously measuring the 3D orientations and 3D positions of fluorescent molecules,” offering details on the dipole-spread function optimization algorithm, estimation algorithm, instrument alignment, system calibration, sample preparation, and additional data analysis.

---

## Contents

1	Imaging model and pixOL algorithm	2	S5	Image plane basis images $\mathbf{B}$ of the pixOL DSF . . . .	10
2	Single-molecule detection and 3D orientation and 3D position estimation	3	S6	Optimizing phase masks for various signal to background ratios . . . . .	11
3	Quantifying the precision of measuring 3D orientation and 3D position	4	S7	Orientation estimation precision of pixOL phase masks compared to back focal plane imaging . . . .	11
4	Quantifying estimation bias when measuring 3D orientation and 3D position	6	S8	Estimation precision of pixOL compared to other 3D orientation imaging techniques . . . . .	12
5	Optical instrumentation and alignment	6	S9	Orientation estimation precision of pixOL for emitters at various axial locations . . . . .	12
6	Imaging system calibration	6	S10	Change in image plane basis images $\mathbf{B}$ with respect to emitter position . . . . .	12
7	Preparing 3D spherical supported lipid bilayers	6	S11	Accuracy of the first-order approximation of the pixOL DSF . . . . .	13
8	Imaging spherical lipid bilayers using Nile red	7	S12	Average basis images $\mathbf{B}_a$ used for detecting single molecules . . . . .	13
			S13	Single-molecule detection and position estimation using the pixOL microscope . . . . .	14
			S14	Coupling between different position and orientation parameters for pixOL . . . . .	14
			S15	Influence of orientation-position correlations on measurement precision. . . . .	14
			S16	Precision and accuracy of estimating 3D orientation and 3D position for emitters at $h = 0$ nm with low background . . . . .	15
			S17	Precision and accuracy of estimating 3D orientation and 3D position for emitters at $h = 400$ nm with low background . . . . .	16
			S18	Precision and accuracy of estimating 3D orientation and 3D position for emitters at $h = 700$ nm with low background . . . . .	17
			S19	Precision and accuracy of estimating 3D orientation and 3D position for emitters at $h = 700$ nm after filtering biased estimates . . . . .	18

## List of Tables

S1	Measurement precision of pixOL compared to other techniques . . . . .	8
----	---	---

## List of Figures

S1	Imaging system schematic . . . . .	8
S2	Basis images $\mathbf{B}_{\text{BFP}}$ at the back-focal plane of an x-y polarized microscope . . . . .	9
S3	Effect of modulating super-critical fluorescence differently from sub-critical fluorescence . . . . .	9
S4	Comparison between pixel-based optimization and Zernike polynomial based optimization . . . . .	10

S20	Precision and accuracy of estimating 3D orientation and 3D position for emitters at $h = 0$ nm with high background . . . . .	19
S21	Precision and accuracy of estimating 3D orientation and 3D position for emitters at $h = 400$ nm with high background . . . . .	20
S22	Precision and accuracy of estimating 3D orientation and 3D position for emitters at $h = 700$ nm with high background . . . . .	21
S23	Precision and accuracy of estimating 3D orientation and 3D position for emitters at $h = 400$ nm with a nominal focal plane placed at $z = -580$ nm. . . . .	22
S24	Correlation between measurements of 3D orientation and 3D position for emitters near $h = 700$ nm . . . . .	23
S25	Aligning the spatial light modulator . . . . .	23
S26	Calibration of the pixOL phase mask . . . . .	24
S27	Calibration of the conjugate pixOL* phase mask . . . . .	25
S28	Comparison between calibrated phase masks and their smoothed versions for pixOL and pixOL* . . . . .	26
S29	Image plane basis images $\mathbf{B}$ of the pixOL DSF at different wavelengths . . . . .	27
S30	Position and emission anisotropy measurements of two fluorescent beads . . . . .	28
S31	Photophysics of Nile red blinking events . . . . .	28
S32	6D SMOLM imaging of Nile red within a spherical bilayer (DPPC with cholesterol) . . . . .	29
S33	6D SMOLM imaging of Nile red within a spherical bilayer (DPPC only) . . . . .	30

## List of Movies

S1	Demonstration of SM detection and position-orientation estimation using the pixOL microscope . . . . .	31
S2	3D view of 6D SMOLM imaging of Nile red within spherical supported lipid bilayers . . . . .	31
S3	x-y cross-sections of 6D SMOLM imaging of Nile red within spherical supported lipid bilayers . . . . .	31

## 1. IMAGING MODEL AND PIXOL ALGORITHM

The goal of the pixOL algorithm is to simultaneously optimize all pixels of a phase mask  $\mathbf{P} \in \mathbb{R}^{n \times n}$  so that the resulting dipole-spread function (DSF) has optimal precision for measuring the 3D orientation  $[\mu_x, \mu_y, \mu_z, \Omega]$  of dipole-like emitters. The dipole's average orientation  $(\theta, \phi)$  in spherical coordinates during a camera frame is related to its unit vector parameterization  $\boldsymbol{\mu} = [\mu_x, \mu_y, \mu_z]^T$  in Cartesian space by

$$[\mu_x, \mu_y, \mu_z] = [\sin \theta \cos \phi, \sin \theta \sin \phi, \cos \theta]. \quad (\text{S1})$$

A wobbling dipole with the orientation parameters  $[\mu_x, \mu_y, \mu_z, \Omega]$ , where the solid angle  $\Omega$  characterizes rotational diffusion within a hard-edged cone, may be characterized using the six orientational second moments  $\mathbf{m} \in \mathbb{R}^6$  as [1, 2]

$$\mathbf{m} = [\langle \mu_x^2 \rangle, \langle \mu_y^2 \rangle, \langle \mu_z^2 \rangle, \langle \mu_x \mu_y \rangle, \langle \mu_x \mu_z \rangle, \langle \mu_y \mu_z \rangle]^T \quad (\text{S2})$$

where

$$\langle \mu_x^2 \rangle = \gamma \mu_x^2 + (1 - \gamma)/3, \quad (\text{S3a})$$

$$\langle \mu_y^2 \rangle = \gamma \mu_y^2 + (1 - \gamma)/3, \quad (\text{S3b})$$

$$\langle \mu_z^2 \rangle = \gamma \mu_z^2 + (1 - \gamma)/3, \quad (\text{S3c})$$

$$\langle \mu_x \mu_y \rangle = \gamma \mu_x \mu_y, \quad (\text{S3d})$$

$$\langle \mu_x \mu_z \rangle = \gamma \mu_x \mu_z, \quad (\text{S3e})$$

$$\langle \mu_y \mu_z \rangle = \gamma \mu_y \mu_z, \quad (\text{S3f})$$

$$\gamma = 1 - \frac{3\Omega}{4\pi} + \frac{\Omega^2}{8\pi^2}. \quad (\text{S3g})$$

We optimize the phase mask for a microscope that splits the collected fluorescence into x- and y-polarized channels (Fig. 1(a)). To model such a system, we begin by writing the x- and y-polarized electric field  $\mathbf{E}_{\text{BFP}}$  at the back focal plane (BFP) as [1, 3–5]

$$\mathbf{E}_{\text{BFP}}(u, v) = \exp\left(jk_1 z \sqrt{1 - (u^2 + v^2)}\right) \exp\left(jk_h h \sqrt{1 - \frac{n_1^2}{n_h^2}(u^2 + v^2)}\right) \begin{bmatrix} g_{x,\text{BFP}}^{(x)}(u, v) & g_{y,\text{BFP}}^{(x)}(u, v) & g_{z,\text{BFP}}^{(x)}(u, v) \\ g_{x,\text{BFP}}^{(y)}(u, v) & g_{y,\text{BFP}}^{(y)}(u, v) & g_{z,\text{BFP}}^{(y)}(u, v) \end{bmatrix} \begin{bmatrix} \mu_x \\ \mu_y \\ \mu_z \end{bmatrix}, \quad (\text{S4})$$

where  $g_{i,\text{BFP}}^{(l)}$  are the basis fields observed in an  $l$ -polarized BFP from a dipole at axial position  $h$  with orientation  $\mu_i$  [1, 3–5] and  $i, l \in \{x, y, z\}$ . The objective is focused at a nominal focal plane positioned at a distance  $-z$  above the coverslip. The wavenumber  $k_h = n_h 2\pi/\lambda$  represents the wave propagation constant in a sample with refractive index of  $n_h$  (assumed to be water in each of our experiments,  $n_h = 1.33$ ), and the wavenumber  $k_1 = n_1 2\pi/\lambda$  represents the wave propagation constant in immersion oil with refractive index of  $n_1 = 1.518$ . The BFP coordinates are normalized such that  $u^2 + v^2 < 1$ . To optimize both axial precision and orientation precision across a large axial range, the trade-offs between the multi-parameter optimization goals must be balanced. In this work, the pixOL phase mask is optimized for in-focus emitters at the water-glass interface ( $z = h = 0$  nm).

For computational convenience, we move to a discrete model  $\mathbf{g}_i$  of the basis fields, sampling the BFP with sufficient pixels and zero-padding to match the spatial light modulator (SLM) of our imaging system. We concatenate the polarized basis fields  $[\mathbf{g}_i^{(x)}, \mathbf{g}_i^{(y)}]^T$  at the image plane of the microscope and express them jointly as

$$\mathbf{g}_i = \begin{bmatrix} \mathbf{g}_i^{(x)} \\ \mathbf{g}_i^{(y)} \end{bmatrix} = \mathcal{F} \left\{ \begin{bmatrix} \exp(j\mathbf{P}) \\ \exp(j\mathbf{P}) \end{bmatrix} \odot \begin{bmatrix} \mathbf{g}_{i,\text{BFP}}^{(x)} \\ \mathbf{g}_{i,\text{BFP}}^{(y)} \end{bmatrix} \right\}, \quad (\text{S5})$$

where  $\mathcal{F}\{\cdot\}$  denotes a discrete 2D Fourier transform,  $\odot$  represents element-wise multiplication of two vectors or matrices. We may now calculate the basis images  $\mathbf{B} = [\mathbf{B}_{xx}, \mathbf{B}_{yy}, \mathbf{B}_{zz}, \mathbf{B}_{xy}, \mathbf{B}_{xz}, \mathbf{B}_{yz}] \in \mathbb{R}^{N \times 6}$  in the image plane as

$$\mathbf{B}_{xx} = \mathbf{g}_x \odot \mathbf{g}_x^* \quad (\text{S6a})$$

$$\mathbf{B}_{yy} = \mathbf{g}_y \odot \mathbf{g}_y^* \quad (\text{S6b})$$

$$\mathbf{B}_{zz} = \mathbf{g}_z \odot \mathbf{g}_z^* \quad (\text{S6c})$$

$$\mathbf{B}_{xy} = \mathbf{g}_x \odot \mathbf{g}_y^* + \mathbf{g}_x^* \odot \mathbf{g}_y \quad (\text{S6d})$$

$$\mathbf{B}_{xz} = \mathbf{g}_x \odot \mathbf{g}_z^* + \mathbf{g}_x^* \odot \mathbf{g}_z \quad (\text{S6e})$$

$$\mathbf{B}_{yz} = \mathbf{g}_y \odot \mathbf{g}_z^* + \mathbf{g}_y^* \odot \mathbf{g}_z. \quad (\text{S6f})$$

These images  $\mathbf{B}_{il}$  correspond to the DSF (Eqn. 1) produced by a dipole with an orientational second moment  $m_{il}$ , where  $i, l \in \{x, y, z\}$ . A similar expression can be derived for the basis images  $\mathbf{B}_{\text{BFP}}$  in the back focal plane (Fig. S2).

To calculate the best possible precision for estimating the orientational moments  $\mathbf{m}$ , we calculate the Cramér-Rao bound (CRB) matrix  $\mathbf{K}$  using

$$\mathbf{K} = \left( \sum_{j=1}^N \frac{s_j^2}{I_j} \mathbf{B}_j^T \mathbf{B}_j \right)^{-1}, \quad (\text{S7})$$

where  $\mathbf{B}_j \in \mathbb{R}^{1 \times 6}$  is the  $j^{\text{th}}$  row of  $\mathbf{B}$ , the superscript  $T$  denotes a matrix transpose. We wish to find an optimal DSF that minimizes  $\mathbf{K}$  for any possible orientation  $[\mu_x, \mu_y, \mu_z, \Omega]$ , so we build our loss function  $\ell$  (Eqn. 2) to represent the sum of the precision of second moments over a uniformly sampled orientation space  $\mathbb{M}$ . The mean orientation  $\boldsymbol{\mu} = [\mu_x, \mu_y, \mu_z]^T$  is sampled using [6]

$$\mu_x = 2x_1 \sqrt{1 - x_1^2 - x_2^2} \quad (\text{S8a})$$

$$\mu_y = 2x_2 \sqrt{1 - x_1^2 - x_2^2} \quad (\text{S8b})$$

$$\mu_z = 1 - 2(x_1^2 + x_2^2), \quad (\text{S8c})$$

where  $x_1, x_2$  are uniformly distributed within  $(-1, 1)$  and points for which  $x_1^2 + x_2^2 \geq 1$  are rejected. The wobbling angle  $\Omega$  is uniformly sampled within  $[0, 2\pi]$ .

Using GradientTape for automatic differentiation in Tensorflow, we can easily calculate the gradient  $\mathbf{D}$  of the loss function  $\ell$  with respect to the current phase mask  $\mathbf{P}$ . We optimize the mask for dipole emitters located at the glass-water interface with 380 total signal photons detected and 2 background photons in each pixel. To begin, we randomly initialize the phase of each pixel. Updating the current phase mask using the Adam algorithm with a learning rate of 0.05 and a total of 300 iterations, the pixOL algorithm produces a phase mask  $\exp(j\mathbf{P})$  shown in Fig. 1(c) and Fig. S6(b).

## 2. SINGLE-MOLECULE DETECTION AND 3D ORIENTATION AND 3D POSITION ESTIMATION

Detecting single molecules (SMs) and estimating their 3D positions and orientations (6 second moments  $\mathbf{m}$ ) can be computationally expensive and non-convex. We overcome these challenges by 1) applying a linear approximation to the forward imaging model and 2) separating the detection and estimation process into sequential steps.

To begin, we extend the forward model (Eqn. 1) to accommodate images containing  $Q \geq 1$  SMs such that

$$\mathbf{I} = \sum_q s_q \mathbf{B}(x_q, y_q, h_q) \mathbf{m}_q + \mathbf{b}, \quad (\text{S9})$$

where  $s_q$  is the brightness in photons,  $[x_q, y_q, h_q]$  is the 3D location, and  $\mathbf{m}_q$  is the orientational second moment vector of the  $q^{\text{th}}$  emitter.

The basis images  $\mathbf{B}$  change shape for SMs at different axial locations, but only shifts linearly for SMs at different lateral positions. To reduce the computational burden of 3D localization, we discretize the continuous 3D location space using a first-order polynomial approximation. Our imaging model becomes

$$\begin{aligned} \mathbf{I} = & \sum_q \left[ s_q \mathbf{B}(x_{q0}, y_{q0}, h_{q0}) \mathbf{m}_q \right. \\ & + s_q \frac{\partial \mathbf{B}(x_{q0}, y_{q0}, h_{q0})}{\partial x} \mathbf{m}_q dx_q + s_q \frac{\partial \mathbf{B}(x_{q0}, y_{q0}, h_{q0})}{\partial y} \mathbf{m}_q dy_q \\ & \left. + s_q \frac{\partial \mathbf{B}(x_{q0}, y_{q0}, h_{q0})}{\partial h} \mathbf{m}_q dh_q \right] + \mathbf{b}, \quad (\text{S10}) \end{aligned}$$

where  $[x_{q0}, y_{q0}, h_{q0}]$  is the closest discrete grid point to the continuous location  $[x_q, y_q, h_q]$ . The off-grid distances  $[dx_q, dy_q, dh_q] =$

$[x_q, y_q, h_q] - [x_{q0}, y_{q0}, h_{q0}]$  characterize the difference between the true position and the closest grid point. As the last three columns (i.e., images) of the basis matrix  $\mathbf{B}$  have a total energy of zero (Fig. S5), we can further simplify the forward model by excluding these last three images in the first-order approximation. The forward model becomes

$$\mathbf{I} = \sum_q \mathbf{A}_q \boldsymbol{\zeta}_q + \mathbf{b}, \quad (\text{S11})$$

where

$$\mathbf{A}_q = \left[ \mathbf{B}(x_{q0}, y_{q0}, h_{q0}), \frac{\partial \mathbf{B}^o(x_{q0}, y_{q0}, h_{q0})}{\partial x}, \frac{\partial \mathbf{B}^o(x_{q0}, y_{q0}, h_{q0})}{\partial y}, \frac{\partial \mathbf{B}^o(x_{q0}, y_{q0}, h_{q0})}{\partial h} \right], \quad (\text{S12a})$$

$$\boldsymbol{\zeta}_q = \left[ s_q \mathbf{m}_q^T, s_q (\mathbf{m}_q^o)^T dx_q, s_q (\mathbf{m}_q^o)^T dy_q, s_q (\mathbf{m}_q^o)^T dh_q \right]^T, \quad (\text{S12b})$$

the basis matrix  $\mathbf{B}^o$  excludes the last three basis images (Fig. S10), and the second moment vector  $\mathbf{m}_q^o$  excludes the last three elements. Importantly, the matrix  $\mathbf{A}_q$  may be precomputed for a specific imaging system and choice of location grid, while  $\boldsymbol{\zeta}_q$  contains the molecular brightness, orientation, and position information we wish to estimate. Here, we set the grid spacing to  $[p_x = 58.5, p_y = 58.5, p_h = 50]$  nm along the x, y, and h directions. With this grid size, the approximated pixOL DSF is very similar to that using a fully accurate model (Fig. S11). The chosen grid size balances computational speed and accuracy; approximation errors can be reduced by using smaller grid sizes at the cost of computational burden. Thus, we have simplified our 3D orientation and 3D position estimation problem to use a linear forward model (Eqn. S11) involving only 15 elements in  $\boldsymbol{\zeta}_q$  for each emitter, i.e., 6 brightness-weighted second moments at each spatial grid point plus 3 brightness- and moment-weighted first-order distances for each off-grid direction. For comparison, the original first-order approximation model in Eqn. S10 involves 24 parameters for each SM.

We perform detection and estimation as separate tasks involving three main parts. We start by determining the number of emitters and their 2D locations within an image. In the second step, we obtain an initial estimate of an emitter's 3D orientation and 3D position based on cropped images centered at each detected SM. Finally, the algorithm updates the estimates of all emitters simultaneously using the entire image.

To simplify the detection process, we ignore the axial dimension and begin with a 2D forward model

$$\mathbf{I}^{2D} = \sum_q \boldsymbol{\zeta}_q^{2D} \mathbf{A}_q^{2D} + \mathbf{b}, \quad (\text{S13})$$

where

$$\mathbf{A}_q^{2D} = \left[ \mathbf{B}_a(x_{q0}, y_{q0}), \frac{\partial \mathbf{B}_a^o(x_{q0}, y_{q0})}{\partial x}, \frac{\partial \mathbf{B}_a^o(x_{q0}, y_{q0})}{\partial y} \right], \quad (\text{S14a})$$

$$\boldsymbol{\zeta}_q^{2D} = \left[ s_q \mathbf{m}_q^T, s_q (\mathbf{m}_q^o)^T dx_q, s_q (\mathbf{m}_q^o)^T dy_q \right]^T, \quad (\text{S14b})$$

$$\mathbf{B}_a = (\mathbf{B}(x_q, y_q, h_q = 0) + \mathbf{B}(x_q, y_q, h_q = 900 \text{ nm})) / 2, \quad (\text{S14c})$$

and  $\mathbf{B}_a$  is an average basis matrix combining the basis images at the top of the focal volume with the basis images at the bottom axial plane (Fig. S12). We use the RoSE-O algorithm [7], which is designed to detect and estimate the 2D locations and 3D orientations of SMs, to

determine the number of emitters and an initial estimate of their 2D locations  $(\hat{x}_q, \hat{y}_q)$ .

The input image to RoSE-O is concatenated from cropped images collected from the x and y polarization channels as follows. We first use fluorescent beads to generate a polynomial registration map between the two channels. We then manually select the center of the field of view of interest in the y polarization channel. The corresponding center in the x channel is calculated using the registration map. We then crop two images with a small field of view centered at the chosen position within the two polarization channels, and concatenate the two images together to form a single image. This image is then used by RoSE-O to detect SMs and estimate each of their 2D positions and 3D orientations (Fig. S13).

In the second step, we obtain an initial estimate of the 3D orientations and 3D locations of individual emitters. For each detected emitter, we isolate an image of  $21 \times 21$  pixels centered at the grid point  $(\hat{x}_{q0}, \hat{y}_{q0})$  nearest to the estimated 2D location  $(\hat{x}_q, \hat{y}_q)$  from the first step. Using each cropped image  $\mathbf{I}_{\text{det}}$ , algorithm 1 estimates the 15 parameters in  $\zeta_q$  simultaneously by minimizing the negative log-likelihood for  $q^{\text{th}}$  emitter

$$\ell_{\text{NLL},q} = \sum_{i=1}^N \left[ \mathbf{A}_q \zeta_q + \mathbf{b} - \mathbf{I}_{\text{det}} \odot \log(\mathbf{A}_q \zeta_q + \mathbf{b}) \right]_i, \quad (\text{S15})$$

where  $[\cdot]_i$  represents the  $i^{\text{th}}$  element of a vector. In step 3, the estimated  $\zeta_q$  for the  $Q$  SMs are combined as the initial value  $\zeta^0$ . Algorithm 2, based on FISTA [8], is used to refine brightness, position, and orientation estimates  $\zeta_q$  simultaneously for all emitters based on the entire captured image by minimizing the negative log-likelihood for all  $Q$  SMs

$$\ell_{\text{NLL}} = \sum_i^N \left\{ \sum_q (\mathbf{A}_q \zeta_q) + \mathbf{b} - \mathbf{I}_{\text{det}} \odot \log \left[ \sum_q (\mathbf{A}_q \zeta_q) + \mathbf{b} \right] \right\}_i. \quad (\text{S16})$$

The 3D locations  $(\hat{x}_q, \hat{y}_q, \hat{h}_q)$  and orientational moments  $\hat{\mathbf{m}}_q$  of molecule  $q$  can be extracted from  $\zeta_q$  using

$$\hat{\mathbf{s}}_q = \sum_{i=1}^3 \zeta_{q,i}, \quad (\text{S17a})$$

$$\hat{\mathbf{m}}_q = \frac{1}{\hat{\mathbf{s}}_q} \zeta_{q,1:6}, \quad (\text{S17b})$$

$$\hat{x}_q = \hat{x}_{q0} + \frac{\sum_{i=7}^9 \zeta_{q,i}}{\sum_{i=1}^3 \zeta_{q,i}}, \quad (\text{S17c})$$

$$\hat{y}_q = \hat{y}_{q0} + \frac{\sum_{i=10}^{12} \zeta_{q,i}}{\sum_{i=1}^3 \zeta_{q,i}}, \quad (\text{S17d})$$

$$\hat{h}_q = \hat{h}_{q0} + \frac{\sum_{i=13}^{15} \zeta_{q,i}}{\sum_{i=1}^3 \zeta_{q,i}}, \quad (\text{S17e})$$

where  $\zeta_{q,i}$  represents the  $i^{\text{th}}$  element of vector  $\zeta_q$ . The estimated second-moment vectors  $\hat{\mathbf{m}}_q$  are next projected to first-moment orientation space  $(\hat{\phi}, \hat{\theta}, \hat{\Omega})$  using a weighted least-square estimator as follows:

$$(\hat{\phi}, \hat{\theta}, \hat{\Omega}) = \arg \min_{\phi', \theta', \Omega'} (\hat{\mathbf{m}}_q - \mathbf{m}_q(\phi', \theta', \Omega'))^T \mathbf{K}^{-1} (\hat{\mathbf{m}}_q - \mathbf{m}_q(\phi', \theta', \Omega')). \quad (\text{S18})$$

Note that weighting by a Fisher information matrix  $(\mathbf{K}^{-1})$  ensures that more weight is given to the second moments  $m_i$  for which pixOL demonstrates superior precision.

When estimating  $\zeta_q$ , we use two sequential projection operations to enhance the convexity and guarantee that the second-moment  $\hat{\mathbf{m}}_q$  estimates are physically meaningful. The first projection  $P_{L1}$  enforces the first three brightness-weighted moments  $[\zeta_{q,1}, \zeta_{q,2}, \zeta_{q,3}]$  to be positive. It also ensures that the off-grid distances  $[dx_q, dy_q, dh_q]$  are smaller than a threshold  $t$ , since a large off-grid distance will reduce the robustness of the first-order polynomial approximation (Eqn. S10) [9]. Parameters  $[\zeta_{q,i}, d\mathbf{w}_q^i]$  related to each orientational moment  $m_{q,i}$  are projected separately, where

$$i \in \{1, 2, 3\}, \quad (\text{S19a})$$

$$d\mathbf{w}_q^1 = \zeta_{q,[7,10,13]}, \quad (\text{S19b})$$

$$d\mathbf{w}_q^2 = \zeta_{q,[8,11,14]}, \quad (\text{S19c})$$

$$d\mathbf{w}_q^3 = \zeta_{q,[9,12,15]}. \quad (\text{S19d})$$

We write this projection as

$$P_{L1}([\zeta_{q,i}, d\mathbf{w}_q^i]) = \begin{cases} 0, & \text{if } \|d\mathbf{w}_q^i\|_2 \leq \frac{-\zeta_{q,i}}{t} \\ (\zeta_{q,i}, d\mathbf{w}_q^i), & \text{if } \|d\mathbf{w}_q^i\|_2 \leq \zeta_{q,i}t \\ \left( \frac{\zeta_{q,i} + t \|d\mathbf{w}_q^i\|_2}{1+t^2}, \frac{\zeta_{q,i} + t \|d\mathbf{w}_q^i\|_2}{1+t^2} \frac{t d\mathbf{w}_q^i}{\|d\mathbf{w}_q^i\|_2} \right), & \text{if } \|d\mathbf{w}_q^i\|_2 \geq \zeta_{q,i}t, \end{cases} \quad (\text{S20})$$

and  $t = 117$  nm in our case.

The second projection  $P_{L2}$  ensures that the second-moment  $\hat{\mathbf{m}}_q$  estimates correspond to a wobble  $\Omega$  that is physically meaningful, given by

$$P_{L2}(\zeta_q) = [\zeta_{q,1:3}, k\zeta_{q,4:6}, \zeta_{q,7:15}], \quad (\text{S21})$$

where

$$k = \frac{\max(0, \min(1.5e - 0.5, 1))}{1.5e - 0.5}, \quad (\text{S22})$$

and  $e$  is the largest eigenvalue of the second moment matrix.

The algorithm can be modified to estimate the NFP of the objective  $z$  if the axial positions  $h$  of the emitters are known (Figs. 2(e) and S30). If we lack knowledge of both the emitter axial positions and the NFP position, we may “guess” an arbitrary NFP position. Our algorithm will yield an estimated emitter axial position that will simply be shifted by the difference between the hypothetical NFP position and the true NFP position (Fig. S23).

### 3. QUANTIFYING THE PRECISION OF MEASURING 3D ORIENTATION AND 3D POSITION

The Fisher information matrix quantifies the amount of information contained within any DSF regarding the parameters we want to estimate. The shape of the pixOL DSF contains information of both the emitter’s axial location and its 3D orientation. Due to the discrete sampling and finite size of the camera pixels, the off-grid distances  $[dx, dy, dh]$  related to the emitter’s location  $[x, y, h]$  relative to the closest grid point  $[x_0, y_0, h_0]$  also affect the shape of the DSF image. Therefore, the covariance between any pair of position and orientation parameters  $[x, y, h, \theta, \phi, \Omega]$  is nonzero (Fig. S14). Thus, to properly quantify the best-possible precision of measuring 3D position and 3D orientation, while also considering correlations thereof, we calculate Fisher information matrices for joint estimation of 3D position and 3D orientation (Fig. 2(a-d)).

**Algorithm 1.** Estimating the 3D orientation and 3D location of individual emitters based on cropped images

- 1: **input:**  $[I, \mathbf{A}_{\text{library}}]$ 
  - $\triangleright \mathbf{A}_{\text{library}} = [\mathbf{A}_1, \dots, \mathbf{A}_n]$  is a set of basis matrices for emitters located at  $[x, y, h] = \{[0, 0, h_1], \dots, [0, 0, h_n]\}$ , where  $h = [-300, -250, \dots, 1300]$  nm represents the locations of  $n$  h-slices.
- 2: **for**  $j \leftarrow 1$  **to**  $n$  **do**  $\triangleright n$  is the number of h-slices.
- 3:    $\mathbf{A} \leftarrow \mathbf{A}_j$   $\triangleright \mathbf{A}$  represents the current basis matrix.
- 4:   Crop  $\mathbf{A}$  so that each basis image in  $\mathbf{A}$  has a size of  $21 \times 21$  pixels
- 5:    $\zeta_{q,j}^0 \leftarrow \mathbf{A}^{-1}(\mathbf{I} - b)$ 
  - $\triangleright$  Obtain an initial brightness, position, and orientation estimate for the  $q^{\text{th}}$  emitter, assuming its image matches  $\mathbf{A}_j$ .
- 6:   Obtain a refined  $\zeta_{q,j}$ , grid estimation  $w_{q,j}$ , and loss value  $\ell_{\text{NLL},q,j}$  from algorithm 2.
  - $\triangleright$  Use  $\zeta_{q,j}^0$  as the initial value,  $[0, 0, h_j]$  as the initial grid location estimation  $w_{q,j}^0$ , and an iteration number of 30 for algorithm 2.
- 7: **end for**
- 8: Obtain a final estimate  $\zeta_q$  and  $w_q$  from algorithm 2.
  - $\triangleright$  Use  $\zeta_{q,j}$  and  $w_{q,j}$  that has the smallest loss value  $\ell_{\text{NLL},q,j}$  and an iteration number of 100 for algorithm 2.

**Algorithm 2.** Estimating 3D orientation and 3D location using FISTA with backtracking

- 1: **input:**  $[I, \zeta^0, w^0, \mathbf{A}_{\text{library}}, N]$
- 2: Using  $\mathbf{A}_{\text{library}}$ , compute basis matrix  $\mathbf{A}$  centered at the estimated initial grid location  $w^0$ .
- 3:  $w_0 \leftarrow w^0$ ,  $\zeta_0 \leftarrow \zeta^0$ ,  $v_1 \leftarrow \zeta^0$   $\triangleright v_1$  is a nearby point of  $\zeta^0$  that will be used to accelerate the optimization.
- 4:  $t_1 \leftarrow 1$ , and take  $L_0 > 0$  and  $\eta > 1$ .
  - $\triangleright L_0$  denotes a constant chosen for initializing the step size, and  $\eta$  is a constant chosen to adjust step sizes in future steps.
- 5: **for**  $k \leftarrow 1$  **to**  $N$  **do**  $\triangleright N$  is the total number of iterations
- 6:   Calculate the best step size by finding the smallest integer  $i_k > 0$  such that with  $L_k = \eta^{i_k} L_{k-1}$ :  $\ell_{\text{NLL}}(\mathbf{v}_{k,L_k}) \leq \ell_{\text{NLL}}(\mathbf{v}_k) + \nabla_{\mathbf{v}} \ell_{\text{NLL}}(\mathbf{v}_k)^T [\mathbf{v}_{k,L_k} - \mathbf{v}_k] + \frac{L_k}{2} \|\mathbf{v}_{k,L_k} - \mathbf{v}_k\|_2^2$ 
  - $\triangleright \nabla_{\mathbf{v}} \ell_{\text{NLL}}(\mathbf{v}_k) \leftarrow \mathbf{A}^T (1 - (\mathbf{I} \oslash (\mathbf{A}\mathbf{v}_k + \mathbf{b})))$ , and operator  $\oslash$  represents element-wise division of two vectors.
- 7:    $L_k \leftarrow \eta^{i_k} L_{k-1}$
- 8:    $\zeta_k \leftarrow P_{L2}(P_{L1}(\mathbf{v}_k - \frac{1}{L_k} \nabla_{\mathbf{v}} \ell_{\text{NLL}}(\mathbf{v}_k)))$ , and  $P_{L1}$  and  $P_{L2}$  are projection operators shown in Eqn. S20 and Eqn. S21
- 9:   Based on  $\zeta_k$  and  $w_{k-1}$ , compute  $[\hat{x}, \hat{y}, \hat{h}]$  and its closest grid point  $w_k = [\hat{x}_0, \hat{y}_0, \hat{h}_0]$  using Eqn. S17
- 10:   Compute  $\mathbf{A}$  centered at the new grid location  $w_k$  using  $\mathbf{A}_{\text{library}}$ .
- 11:   Compute  $\zeta_{k-1,\text{new}}$  and  $\zeta_{k,\text{new}}$  based on the new grid location  $w_k$ .
  - $\triangleright \zeta_{k-1,\text{new}} = \zeta_{k-1} + [o_0, o_1 \zeta_{k-1,[1:3]}, o_2 \zeta_{k-1,[1:3]}, o_3 \zeta_{k-1,[1:3]}]$ ,  $\zeta_{k,\text{new}} = \zeta_k + [o_0, o_1 \zeta_{k,[1:3]}, o_2 \zeta_{k,[1:3]}, o_3 \zeta_{k,[1:3]}]$ , where  $o_0 = [0, 0, 0, 0, 0]$ ,  $o_1 = (w_{k-1,1} - w_{k,1})$ ,  $o_2 = (w_{k-1,2} - w_{k,2})$ ,  $o_3 = (w_{k-1,3} - w_{k,3})$
- 12:    $\zeta_{k-1} \leftarrow \zeta_{k-1,\text{new}}$ , and  $\zeta_k \leftarrow \zeta_{k,\text{new}}$
- 13:    $t_k \leftarrow \frac{1 + \sqrt{1 + 4t_k^2}}{2}$
- 14:    $v_{k+1} \leftarrow \zeta_k + \frac{t_k - 1}{t_{k+1}} (\zeta_k - \zeta_{k-1})$
- 15: **end for**

For Fig. 2(a,b), we calculate a  $6 \times 6$  Fisher information matrix that includes 3 location and 3 orientation parameters. By inverting the Fisher information matrix, we obtain the CRB matrix  $\mathbf{K}$ , whose diagonal elements quantify the estimation variance of 3D orientation  $[\theta, \phi, \Omega]$  and 3D location  $[x, y, h]$ . To quantify the precision of estimating the mean orientation  $[\theta, \phi]$ , we calculate the angular precision  $\sigma_\delta$ , which is the half-angle of the uncertainty cone for estimating the mean orientation direction [10]. It is a summary metric that combines the precision  $\sigma_\theta$  of measuring  $\theta$  and the standard deviation  $\sigma_\phi$  of measuring  $\phi$ , given by

$$\sigma_\delta = 2 \arcsin \left( \sqrt{\frac{\sin(\theta) \sqrt{\det(\mathbf{K}_{4:5,4:5})}}{4\pi}} \right), \quad (\text{S23})$$

where  $\mathbf{K}_{4:5,4:5}$  is a  $2 \times 2$  sub-matrix of  $\mathbf{K}$  representing 3D orientation  $[\theta, \phi]$  precision formed by fourth and fifth rows and columns. We sample orientation space  $(\theta, \phi)$  uniformly using

$$\phi = 2\pi v_1, \quad (\text{S24})$$

$$\theta = \arccos(2u_1 - 1), \quad (\text{S25})$$

where  $v_1, u_1$  are uniformly distributed on  $(0,1)$ . The angular precision  $\sigma_\delta$  and wobbling angle precision  $\sigma_\Omega$  is then averaged over all  $\theta$  in Fig. 2(a,b).

To quantify 3D location precision for isotropic emitters (Fig. 2(c,d)), we build a  $9 \times 9$  Fisher information matrix, which includes the 3 location parameters and 6 orientational moments. This formulation avoids the undefined mean orientation direction  $(\theta, \phi)$  of these emitters.

The correlation between the 3D orientation and 3D location will degrade estimation precision in general. We quantify the difference ratio  $Y$  between the precision calculated with orientation-position correlation and without using

$$Y(\sigma) = \frac{\sigma_{\text{with correlation}} - \sigma_{\text{without correlation}}}{\sigma_{\text{without correlation}}}, \quad (\text{S26})$$

where  $\sigma_{\text{without correlation}}$  is calculated using matrices  $\mathbf{K}$  that quantify solely 3D localization precision or 3D orientation measurement precision. We noticed that the performance of large DSFs (i.e., those that

are greater than 3 times the size of the standard PSF) is less influenced by orientation-position correlations (Fig. S15).

#### 4. QUANTIFYING ESTIMATION BIAS WHEN MEASURING 3D ORIENTATION AND 3D POSITION

To determine if correlations between measurements of 3D orientation and 3D position influence estimation performance, we simulated images of emitters with various orientations and axial locations and a nominal focal plane set to  $z = -580$  nm (Figs. S16-S22). For each configuration, 200 independent images are simulated using the forward model (Eqn. 1) and estimated using algorithm described in Section 2. Overall, pixOL shows excellent precision for measuring 3D orientation and 3D position. However, in some regions of the orientation domain, we notice low estimation precision and accuracy for both 3D orientation and 3D position. Plotting the estimates in one of these regions, we notice strong correlations between biases in 3D orientations and biases in 3D locations (Fig. S24(a,b)). For example, simulated noiseless images of an emitter at the ground truth position  $(x_0, y_0, h_0) = (0, 0, 700)$  nm and orientation  $(\theta_0, \phi_0, \Omega_0) = (38^\circ, 162^\circ, 0)$  are very similar to those of a biased estimate of position and orientation (Fig. S24(c,d)). However, differences between the noisy images are still discernible. We suspect that position-orientation correlations create local minima in the likelihood space.

We note that to make high-dimensional parameter estimation computationally feasible, our algorithm iteratively updates its approximate forward model based on its current 3D position estimate (Algorithm 2, step 10). This strategy leads to a non-continuous optimization surface and increases the difficulty for our algorithm to jump out of local minima. It is possible that a neural network-based algorithm will be more computationally efficient and may be able to explore the 6D position-orientation space more robustly. Such an approach could increase estimation precision and remove bias (Fig. S24(e)).

#### 5. OPTICAL INSTRUMENTATION AND ALIGNMENT

The pixOL DSF is implemented using a home-built epifluorescence microscope as described previously [2, 11]. Briefly, a polarization-resolved 4f imaging system, consisting of relay lenses and a polarizing beamsplitter, is appended to a fluorescence microscope to project two polarized images onto separate regions of a camera (Fig. S1). A spatial light modulator (SLM, Meadowlark Optics, 256 XY Phase Series) is placed at the conjugate back focal plane (BFP) of the imaging system and loaded with the pixOL phase mask to modulate the x- and y-polarized fluorescence simultaneously (Fig. S1 inset(i)(ii)).

To properly align the SLM, we load a binary phase mask consisting of concentric rings of increasing radius (10-pixel interval) centered on the SLM. A dense layer of fluorescent beads (100-nm diameter red 580/605 FluoSpheres, Invitrogen F8801) on a coverslip is used to generate fluorescence for calibration. By using the flipping mirror in Fig. S1, a camera (camera 2 in Fig. S1) placed at a conjugate back focal plane is able to observe the pupil of the objective lens and the SLM ring pattern simultaneously in the y-polarization channel. The axial alignment of the SLM is adjusted until the pupil and rings are sharp simultaneously. The SLM is shifted laterally until the SLM's ring mask is centered with respect to the microscope pupil (Fig. S25). The alignment of the SLM within the x-polarization channel can be verified by adjusting the position of lens 4 and camera 2 in Fig. S1. In our experience, lateral deviations of the SLM up to  $\sim 0.1$  mm are difficult to detect by observing the pixOL DSF itself.

#### 6. IMAGING SYSTEM CALIBRATION

We calibrate the imaging model in Section 2 to the DSF of our imaging system by using fluorescent beads (100-nm diameter red 580/605 FluoSpheres, Invitrogen F8801). Images are captured by scanning the objective's nominal focal plane from  $z = -790$  nm to  $z = 610$  nm with a step size of 50 nm (Figs. S26(e), S27(f), and 2(e)). At each plane, 11 images are taken.

A phase-retrieval algorithm [12] is used to retrieve the experimental phase mask, calibrated pixOL  $\tilde{P}$ . To accurately characterize the optical aberrations of our microscope, the phase masks of the two polarized channels are estimated independently (Figs. S26(b,c) and S27(c,d)). The simulated DSFs using the calibrated phase masks  $\tilde{P}$  match the experimental DSFs very well (Figs. S26(f) and S27(g)).

We performed phase retrieval for both the pixOL phase mask and its conjugate mask (pixOL\*). The retrieval algorithm assumes that the polarized field from a dipole emitter is collected by an ideal objective lens and that the polarizing beam splitter splits x and y-polarized light with a perfect contrast ratio. Thus, we assume that the optical aberrations are strictly phase-only. We notice that the pixOL phase mask's DSF has a large aberration when the objective is focused below the coverslip ( $z > 0$ , Fig. S26(e)). While aberrations also exist in the pixOL\* experimental DSF at the same locations, its mismatch relative to the ideal pixOL DSF is more modest and is similar to spherical aberration (Fig. S27(f)).

We also noticed high frequency patterns in the calibrated phase masks near the edge of the aperture (Figs. S26(b,c) and S27(c,d)). To test if these patterns meaningfully impact the shape of the DSF, we reconstruct smoothed versions of the calibrated phase masks by projecting it into a Zernike basis using the first 231 Zernike polynomials (Fig. S28(a,b)). We calculate the negative-likelihood (NLL, Eqn. S15) between the DSF predicted by each mask and the experimental images of beads used for phase retrieval (Figs. S26(d) and S27(e)). The NLL (NLL<sub>calibrated</sub>) for the calibrated phase masks is always smaller than the NLL (NLL<sub>smoothed</sub>) for the smoothed phase masks (Fig. S28(c,d)). These data indicate that the calibrated masks are more consistent with the experimentally observed DSFs than the smoothed masks.

#### 7. PREPARING 3D SPHERICAL SUPPORTED LIPID BILAYERS

Supported lipid bilayers (SLBs) were formed by fusing vesicles on silica beads. A lipid mixture containing 0.286 mg/mL DPPC (di(16:0) phosphatidylcholine, Avanti Polar Lipids 850355) and 0.1 mg/mL cholesterol (Sigma Aldrich C8667) within Tris buffer (100 mM NaCl, 3 mM  $\text{Ca}^{2+}$ , 10 mM Tris, pH 7.4) is first incubated in a water bath at a temperature of  $65^\circ\text{C}$ . Simultaneously, 1 mg/mL silica beads (2.0  $\mu\text{m}$  diameter, Bangs Laboratories SS04002) are also incubated in the water bath for  $\sim 10$  minutes. After two solutions reach to thermal equilibrium, 30  $\mu\text{L}$  of the lipid mixture and 90  $\mu\text{L}$  of the silica beads are mixed together and stay in the water bath for another 30 minutes. During the 30 minutes, the mixture is vortexed every 5 minutes. The mixture is then moved outside the water bath together with around 200 mL of warm water to allow it to cool down to room temperature for about 1 hour. During this cooling process, the mixture is vortexed every 5 minutes to allow the lipid bilayer to coat the bead uniformly.

After the mixture cool down to the room temperature, we remove the excess vesicles using six successive 5-min centrifuge spins at 500 RPM. The supernatant is discarded and replaced with imaging buffer (100 mM NaCl, 10 mM Tris, pH 7.4) after each spin.

## 8. IMAGING SPHERICAL LIPID BILAYERS USING NILE RED

Nile red (32 nM) is added to the imaging buffer to probe the morphology and composition of the spherical lipid bilayers. We use circularly polarized illumination ( $1533 \text{ W/cm}^2$  or 30 mW at 561 nm at the sample) to excite NR. Fluorescence is collected using an objective lens (OLYMPUS UPLSAPO100XOPSF, NA 1.4) and passes through a dichroic mirror (Di01-R488/561, Semrock) and bandpass filter (FF01-523/610, Semrock). The difference between the basis images of the pixOL DSF for fluorescence at the two edges of the filter (641 nm and 583 nm) is small (peak difference of 8.3%, Fig. S29). The chromatic aberration introduced by the nonzero fluorescence bandwidth is negligible.

We captured 20000 frames with an exposure time of 110 ms. To compensate for axial drift of the microscope during long-term imaging, the objective is refocused every 2000 frames. We use a nominal focal plane (NFP) of  $z = -350 \text{ nm}$  for the DPPC+chol bead and an NFP of  $z = -500 \text{ nm}$  for the DPPC-only bead. The lateral drift of the microscope is corrected after imaging. We aligned the lateral centers of each sphere using SM position estimates averaged in groups of 2000 frames. With these experimental conditions, we observe single-molecule blinking with properties shown in Fig. S31.

To quantify the localization precision for NRs, we plot the NR lateral positions  $r$  relative to the sphere's center within each  $h$  slice (Figs. S32(d) and S33(d)). We compare the experimental distribution to a theoretical distribution  $p_{\text{theo}}$  calculated by convolving the lateral positions  $p_{\text{sphere}}$  representing the spherical surface with the expected lateral localization distribution  $p_{\text{pixOL}^*}$  of pixOL\* based on the CRB when normal focal plane equals to -580 nm, i.e.,

$$p_{\text{theo}}(r) = p_{\text{sphere}} \circledast p_{\text{pixOL}^*}, \quad (\text{S27})$$

where

$$p_{\text{sphere}}(r) = \frac{R}{(\sqrt{R^2 - r^2})}, \quad (\text{S28a})$$

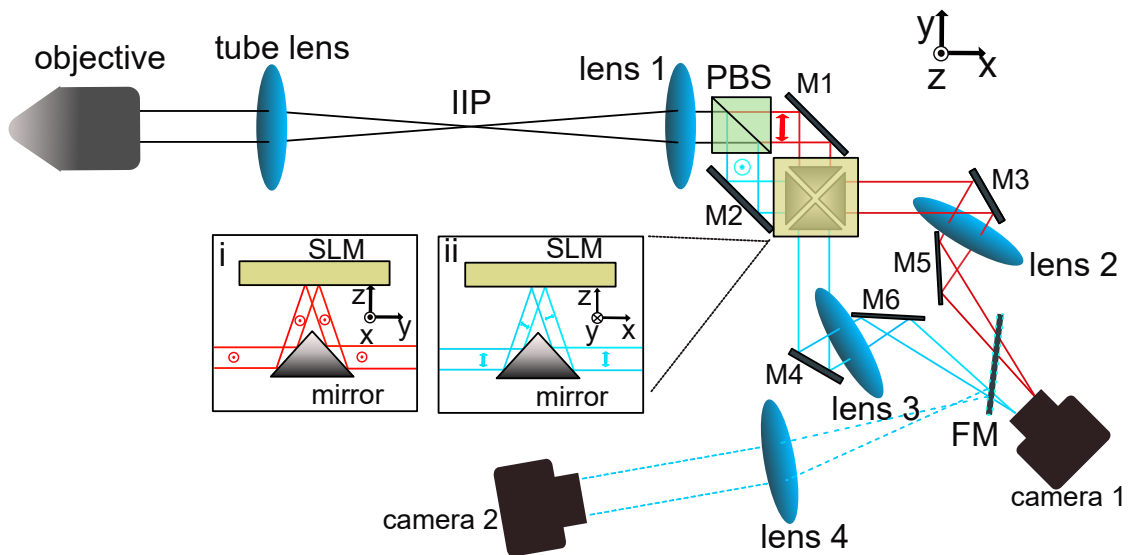
$$p_{\text{pixOL}^*}(r) = \frac{1}{\sigma_L(\sqrt{R^2 - r^2})\sqrt{2\pi}} \times \exp\left[-\frac{1}{2}\left(\frac{r}{\sigma_L(\sqrt{R^2 - r^2})}\right)^2\right], \quad (\text{S28b})$$

$R$  is the radius of the sphere,  $\sigma_L(\sqrt{R^2 - r^2})$  is the lateral precision of pixOL\* for an emitter on the sphere's surface with  $h = R - \sqrt{R^2 - r^2}$ , and  $\circledast$  represents convolution operation.

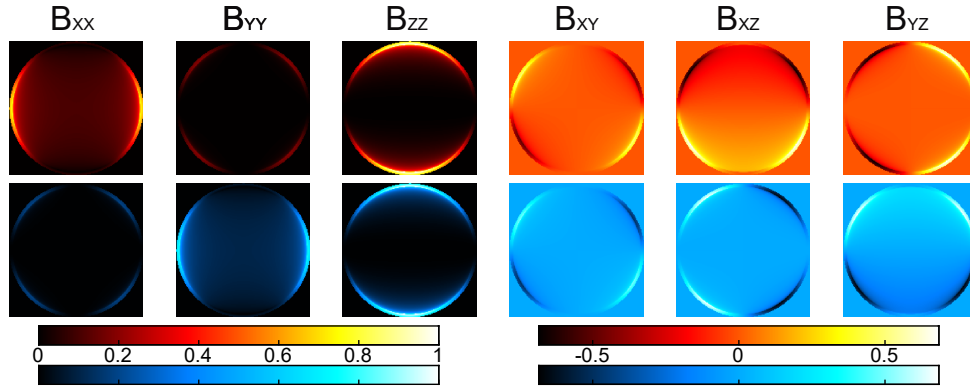


			pixOL	CHIDO	DH	vortex
high SBR (2500:3)	in focus	mean MASD $\sigma_\delta(\circ)$	<u>0.8</u>	1.0	1.4	1.3
		mean wobble angle precision $\sigma_\Omega(\text{sr})$	<u>0.16</u>	0.18	0.32	0.24
	average over a 800-nm axial range	mean MASD $\sigma_\delta(\circ)$	1.1	<u>1.1</u>	1.5	1.7
		mean wobble angle precision $\sigma_\Omega(\text{sr})$	0.24	<u>0.24</u>	0.35	0.36
		mean precision for lateral position $\sigma_L(\text{nm})$	<u>8.2</u>	11.0	12.0	13.4
		mean precision for axial position $\sigma_h(\text{nm})$	12.2	15.8	<u>11.0</u>	14.2
low SBR (2500:10)	in focus	mean MASD $\sigma_\delta(\circ)$	<u>1.1</u>	1.2	2.2	1.7
		mean wobble angle precision $\sigma_\Omega(\text{sr})$	<u>0.23</u>	0.25	0.52	0.33
	average over a 800-nm axial range	mean MASD $\sigma_\delta(\circ)$	1.4	<u>1.4</u>	2.0	2.0
		mean wobble angle precision $\sigma_\Omega(\text{sr})$	0.30	<u>0.30</u>	0.46	0.45
		mean precision for lateral position $\sigma_L(\text{nm})$	<u>11.4</u>	16.2	18.5	20.0
		mean precision for axial position $\sigma_h(\text{nm})$	17.9	23.1	<u>16.9</u>	21.7

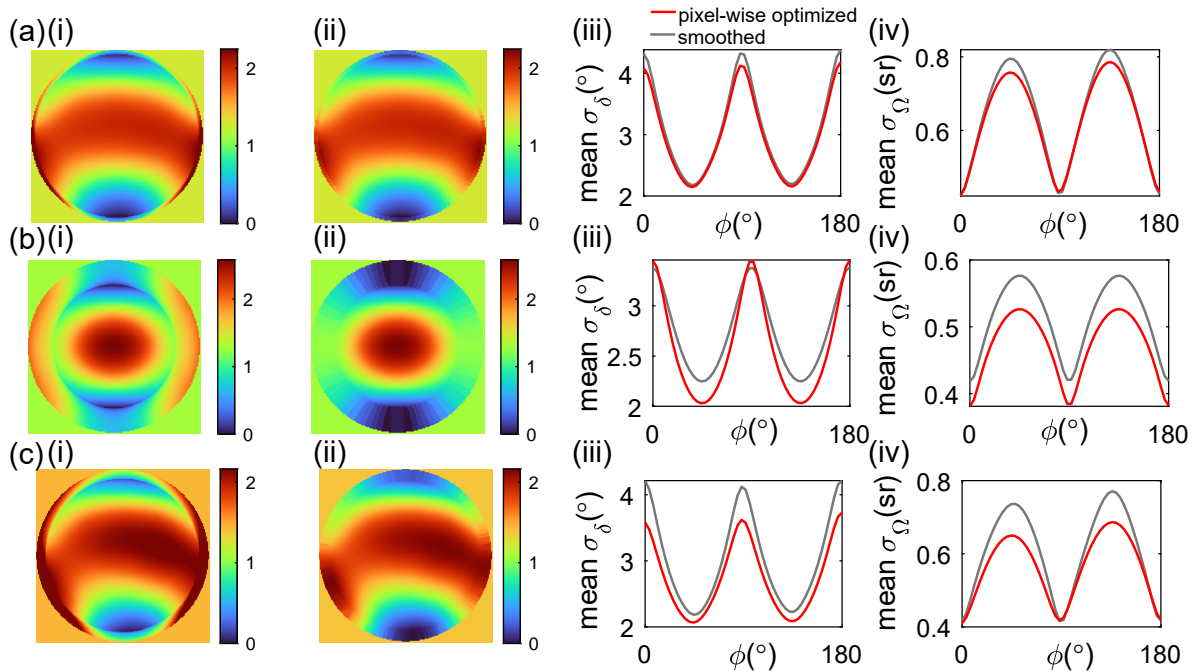
**Table S1.** Measurement precision of pixOL compared to other techniques: CHIDO [13], double helix (DH) [14], and unpolarized vortex [15]. The best-possible measurement precisions are calculated using the Cramér-Rao bound (CRB) for mean orientation angle  $[\theta, \phi]$  (MASD,  $\sigma_\delta$ ), wobble angle  $\sigma_\Omega$ , lateral position  $\sigma_L$ , and axial position  $\sigma_h$ . MASD quantifies the combined precision of measuring  $\theta$  and  $\phi$  as the half-angle of a cone representing orientation uncertainty (Eqn. S23) [10]. The orientation precisions are calculated for fixed emitters ( $\Omega = 0$  sr) and averaged over the whole orientation sphere. The localization precisions are calculated for isotropic emitters ( $\Omega = 2\pi$  sr). Emitters are located within water (1.33 refractive index) with a 2500:3 signal to background ratio (SBR, signal photons:background photons/pixel) and a 2500:10 SBR.



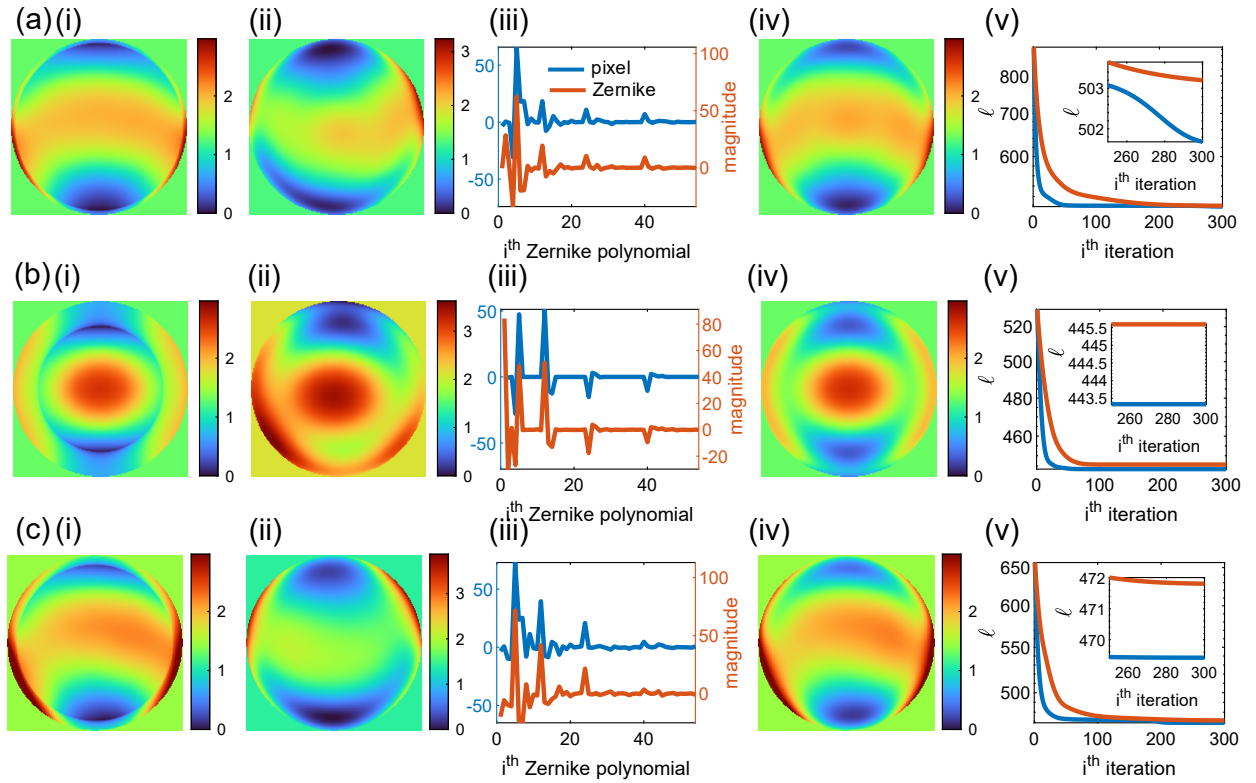
**Fig. S1.** Imaging system schematic. Fluorescence from single molecules is collected by the objective. A polarization-sensitive 4f system, comprising 3 lenses (lenses 1-3) and a polarizing beam splitter (PBS), is added after the microscope's intermediate image plane (IIP). The PBS splits the light into x-polarized (red) and y-polarized (cyan) fluorescence. A pyramid mirror is used to reflect light from two channels onto the spatial light modulator (SLM) placed at the conjugate back focal plane (BFP) of the microscope (insets i and ii). The pixOL phase mask is loaded onto the SLM to modulate the phase of both channels simultaneously. Lenses 2 and 3 focus the x- and y-polarized fluorescence onto two non-overlapping regions of a single CMOS camera (camera 1). Arrows denote the polarization of the light in each channel. The system can be modified to image the BFP by using the flipping mirror (FM). Camera 2 is shown to be imaging the y-polarized BFP, but the x-polarized BFP can be imaged by simply translating the camera appropriately. M1-5, mirrors.



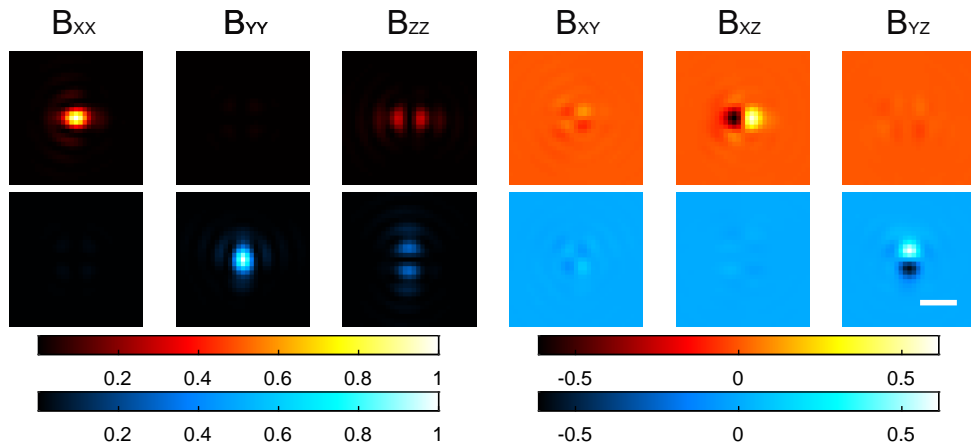
**Fig. S2.** Basis images  $\mathbf{B}_{\text{BFP}}$  at the back-focal plane (BFP) of an x-y polarized microscope (red: x-polarized, blue: y-polarized, Fig. 1(a)). The radius of the circular support in the BFP corresponds to the finite numerical aperture of the microscope's objective lens. The image intensities are normalized relative to the brightest basis image ( $\mathbf{B}_{\text{XX}}$ ). Colorbars: normalized intensity.



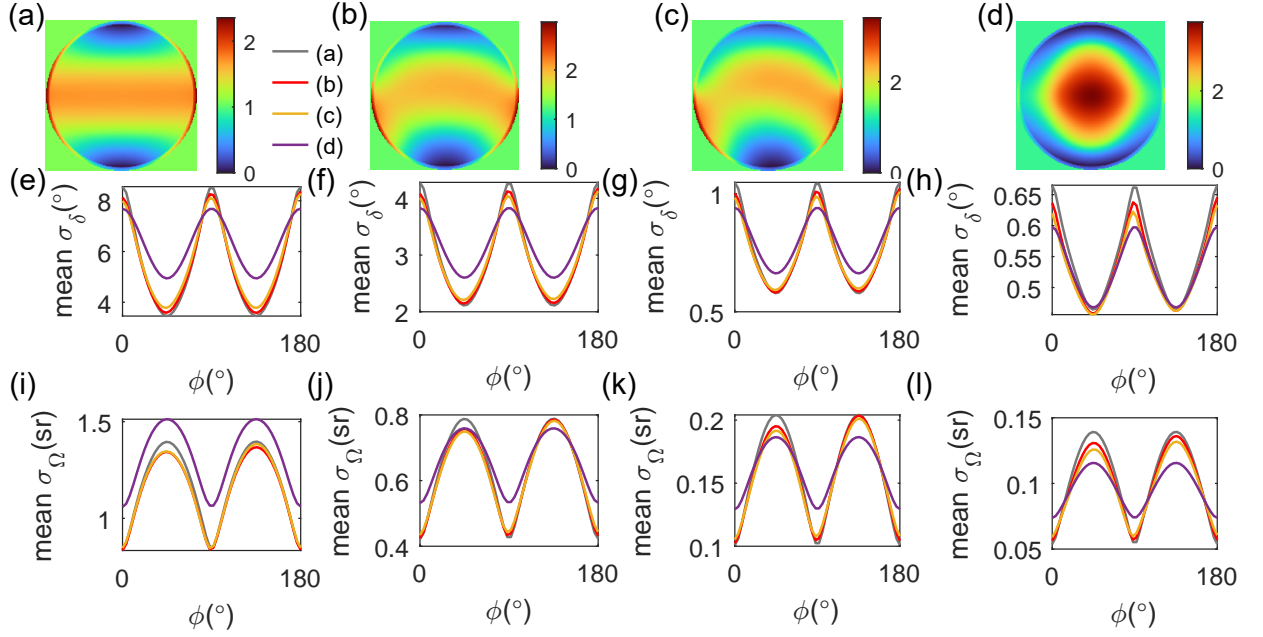
**Fig. S3.** Effect of modulating super-critical fluorescence differently from sub-critical fluorescence. (a-c) (i) Pixel-based optimization for emitters located at the interface between a glass and (a,c) water (refractive index=1.33) or (b) air (refractive index=1). The masks are optimized for an objective with a numerical aperture of (a,b) 1.4 or (c) 1.5. (ii) The super-critical regions of the masks in (i) are smoothed using phase values from the sub-critical regions. (iii) Mean angular standard deviation  $\sigma_\delta$  and (iv) mean wobbling angle precision  $\sigma_\Omega$  averaged over all  $\theta$  for emitters with 380 signal photons and 2 background photons per pixel.



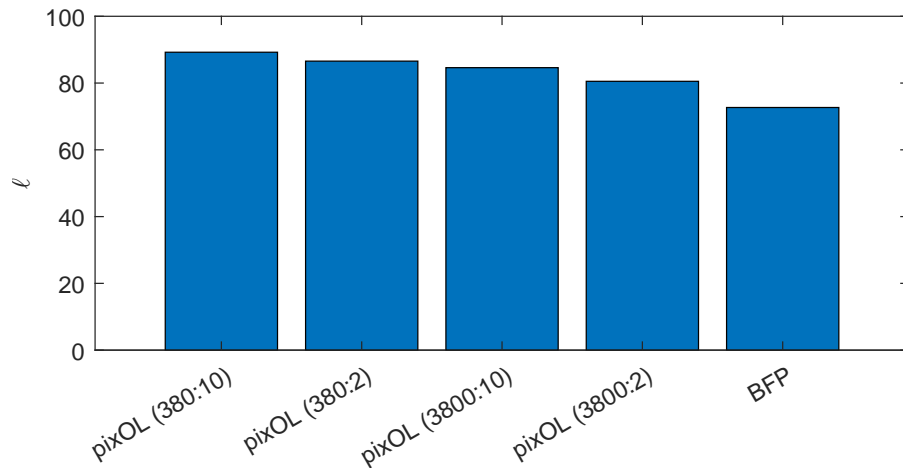
**Fig. S4.** Comparison between pixel-based optimization and Zernike polynomial based optimization. (a-c) (i) Pixel-based optimization and (ii) Zernike polynomial-based optimization for emitters located at the interface between a glass coverslip and (a,c) water (refractive index=1.33) and (b) air (refractive index=1). The masks are optimized for an objective with a numerical aperture of (a,b) 1.4 and (c) 1.5. (iii) Zernike polynomial decompositions of (blue) the pixel-wise optimized mask in (i) and (orange) the Zernike-optimized mask in (ii). Y axis: magnitude of the  $i^{\text{th}}$  Zernike polynomial. (iv) Phase mask reconstructed from the Zernike decomposition (blue curve in (iii)) of the pixel-based optimized phase mask in (i) using the first 55 Zernike polynomials. (iv) Optimization loss curves for the (blue) pixel-wise optimized mask in (i) and (orange) the Zernike-optimized mask in (iii). Inset: the loss curves at the last 50 optimization steps. The loss function is calculated using  $\ell$  (Eqn. 2) for emitters with a total signal photons of 380 and 2 background photons/pixel.



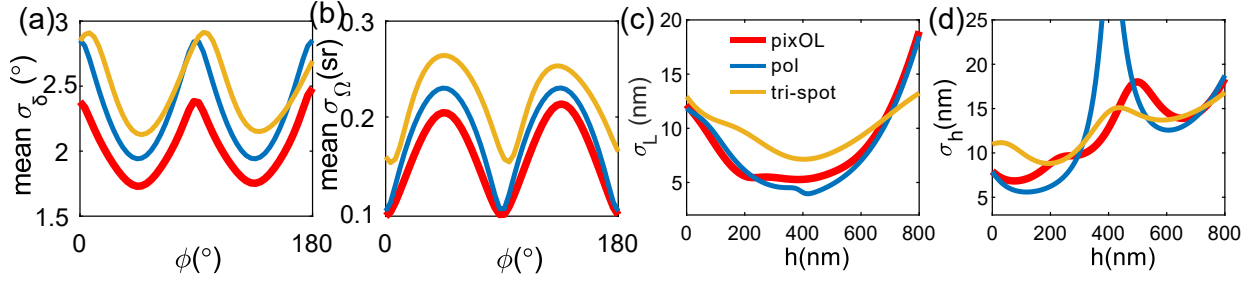
**Fig. S5.** Image plane basis images  $\mathbf{B}$  corresponding to the polarization-sensitive imaging system (red: x-polarized, blue: y-polarized) and pixOL phase mask shown in Fig. 1(a,c) for an in-focus emitter. The image intensities are normalized relative to the brightest basis image ( $\mathbf{B}_{xx}$ ). Colorbars: normalized intensity. Scalebar: 500 nm.



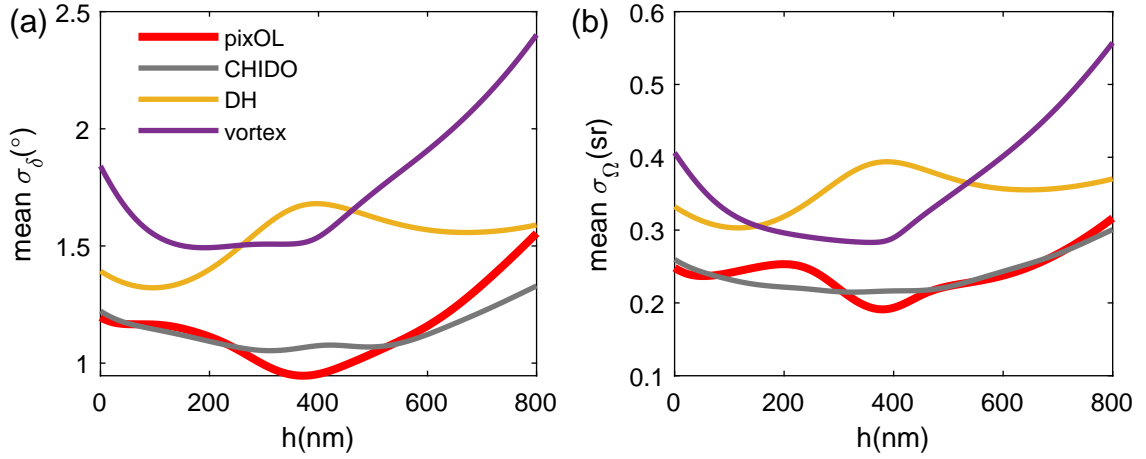
**Fig. S6.** Optimizing phase masks for various signal to background ratios (SBRs, signal photons:background photons/pixel). (a-d) Phase masks optimized for emitters with SBRs of (a) 380:10, (b) 380:2 (matching the design in Fig. 1(c)), (c) 3800:10, and (d) 3800:2. Colorbar: phase (rad). (e-l) Best-possible measurement precision of various engineered DSFs calculated using the Cramér-Rao bound (CRB) for (e-h) mean angular standard deviation  $\sigma_\delta$  and (i-l) mean wobble angle precision  $\sigma_\Omega$  averaged uniformly over all  $\theta$ . Grey: mask in (a), red: mask in (b), yellow: mask in (c), and purple: mask in (d). Precision is calculated for emitters at a water-glass interface with SBRs of (e,i) 380:10, (f,j) 380:2, (g,k) 3800:10, and (h,l) 3800:2.



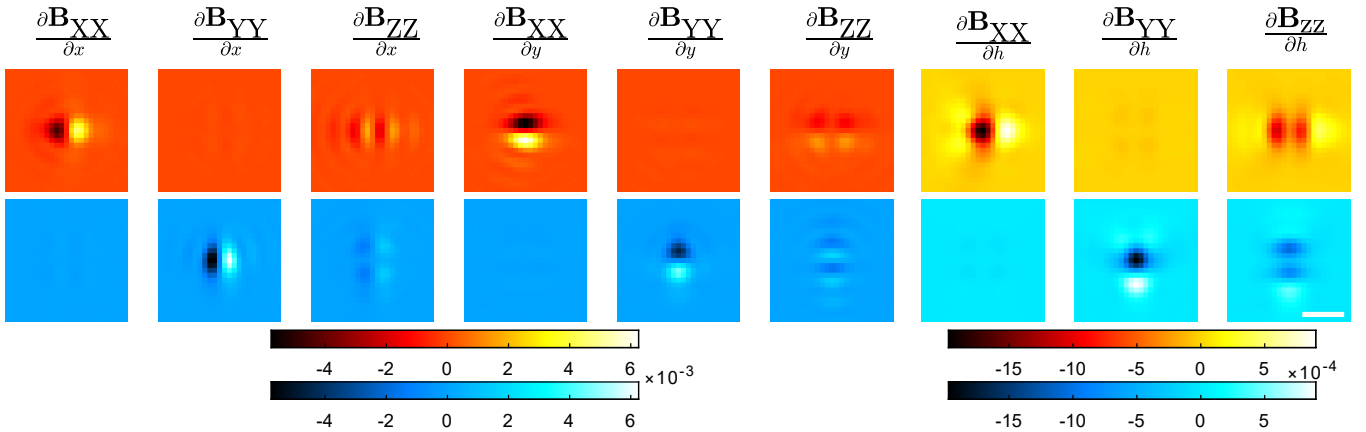
**Fig. S7.** Orientation estimation precision of pixOL phase masks compared to direct back focal plane (BFP) imaging, which achieves performance close to the best-case, quantum-limited orientation measurement precision [16]. Four pixOL masks (Fig. S6(a-d)) are optimized for emitters at various signal to background ratios (SBRs, signal photons:background photons/pixel): 380:10, 380:2, 3800:10, and 3800:2. Orientation precision is calculated using the loss function  $\ell$  (Eqn. 2) for emitters with an SBR of 3800:0.



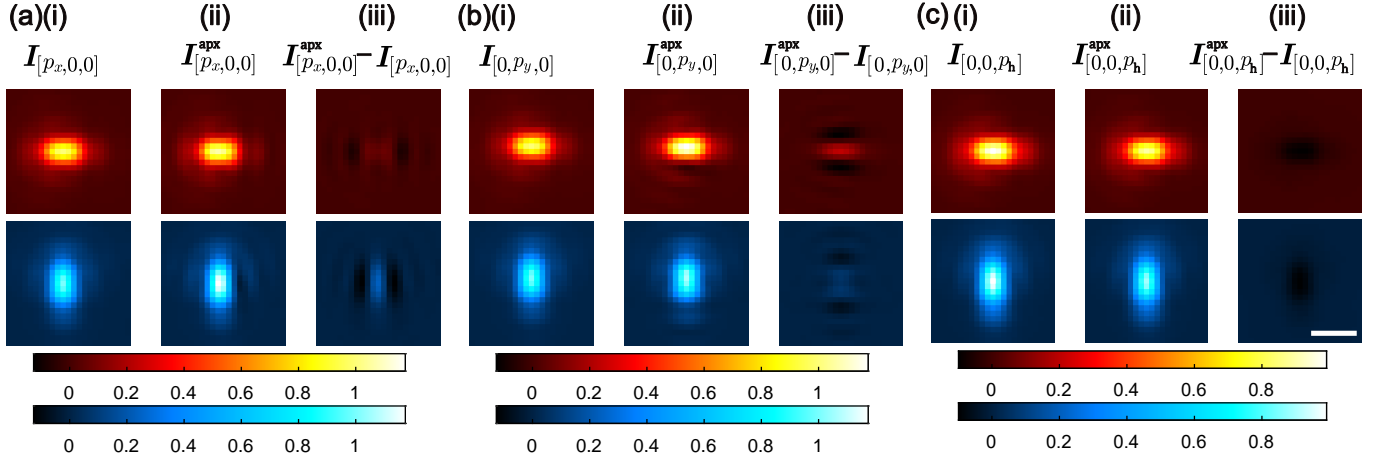
**Fig. S8.** Estimation precision of pixOL compared to techniques designed solely for 3D orientation measurements. Red: pixOL, blue: x-y polarized standard PSF (pol) defocused at 200 nm above the coverslip [17], yellow: tri-spot [18]. (a) Mean angular standard deviation  $\sigma_\delta$  (MASD) averaged uniformly over all  $\theta$ . MASD quantifies the combined precision of measuring  $\theta$  and  $\phi$  as the half-angle of a cone representing orientation uncertainty (Eqn. S23) [10]. (b) Mean wobble angle precision  $\sigma_\Omega$  averaged uniformly over all  $\theta$ . (c,d) Localization precisions  $\sigma_L$  and  $\sigma_h$  for measuring (c) lateral position  $l$  and (d) axial location  $h$  above the interface, respectively. MASD and  $\sigma_\Omega$  are calculated for in-focus SMs with fixed orientation ( $\Omega = 0$  sr); localization precisions are for isotropic emitters ( $\Omega = 2\pi$  sr). Emitters are immersed in water (1.33 refractive index) with 2500 signal photons and 3 background photons per pixel.



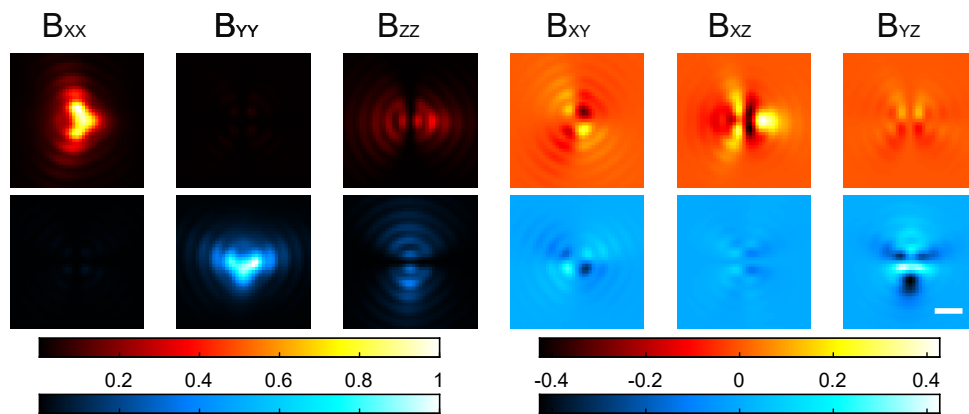
**Fig. S9.** Orientation estimation precision of pixOL for emitters at various axial locations  $h$  compared to techniques designed for 3D orientation and 3D position measurements. Red: pixOL, grey: CHIDO [13], yellow: double helix (DH) [14], purple: unpolarized vortex [15]. (a) Mean angular standard deviation  $\sigma_\delta$  (MASD) averaged uniformly over all  $\theta$  and  $\phi$ . MASD quantifies the combined precision of measuring  $\theta$  and  $\phi$  as the half-angle of a cone representing orientation uncertainty (Eqn. S23) [10]. (b) Mean wobble angle precision  $\sigma_\Omega$  averaged uniformly over all  $\theta$  and  $\phi$ . Emitters have fixed orientations ( $\Omega = 0$  sr), and are immersed in water (1.33 refractive index) with 2500 signal photons and 3 background photons per pixel.



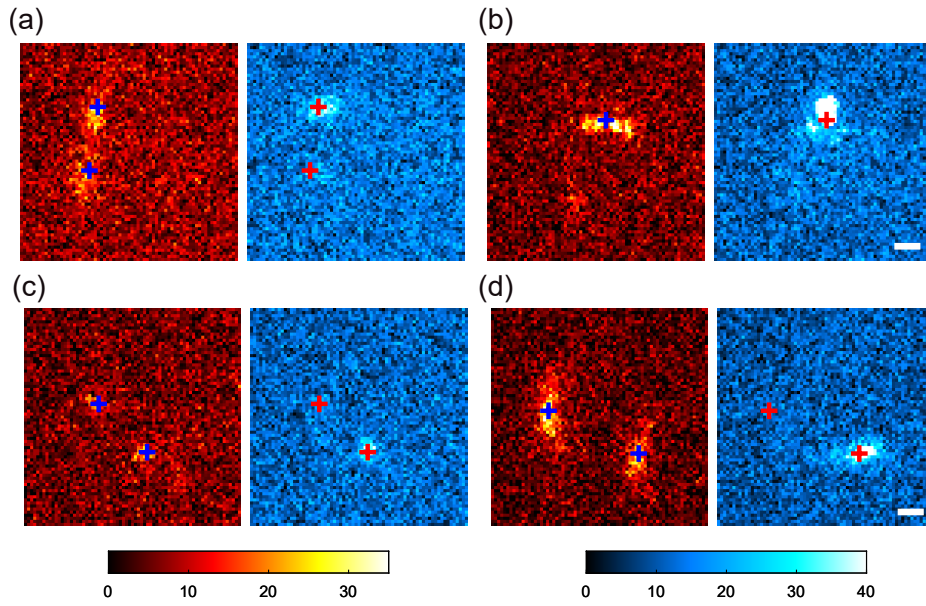
**Fig. S10.** Partial derivatives of the first three basis images ( $B_{XX}$ ,  $B_{YY}$ ,  $B_{ZZ}$ ) in Fig. (S5) with respect to 3D position  $[x, y, h]$ . Colorbars: photons/nm. Scalebar: 500 nm.



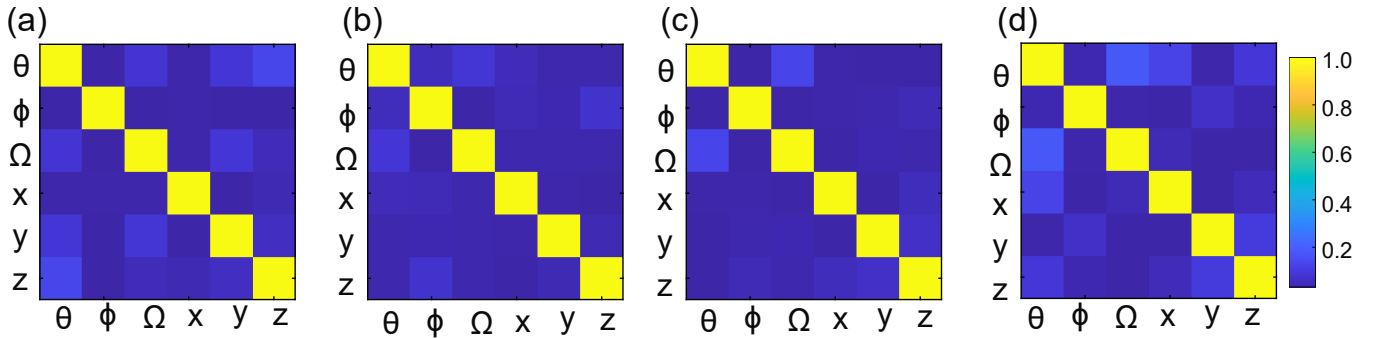
**Fig. S11.** Accuracy of the first-order approximation of the pixOL DSF. (i) Images  $I$  of the pixOL DSF using a fully accurate model for isotropic emitters located at (a)  $[0, 0, p_x]$ , (b)  $[0, p_y, 0]$ , and (c)  $[0, 0, p_h]$ . The grid spacing is given by  $[p_x = 58.5, p_y = 58.5, p_h = 50]$  nm along  $x$ ,  $y$ , and  $h$ . (ii) Images  $I^{\text{apx}}$  of the pixOL DSF using a first-order polynomial approximation (Eqn. S11) for emitters located at positions (a-c) as above. The first-order approximation is evaluated relative to the origin  $[x_0 = 0, y_0 = 0, h_0 = 0]$ . (iii) Difference between  $I$  and  $I^{\text{apx}}$ . Images in each panel are normalized relative to the accurate pixOL DSF  $I$ . Scalebar: 500 nm.



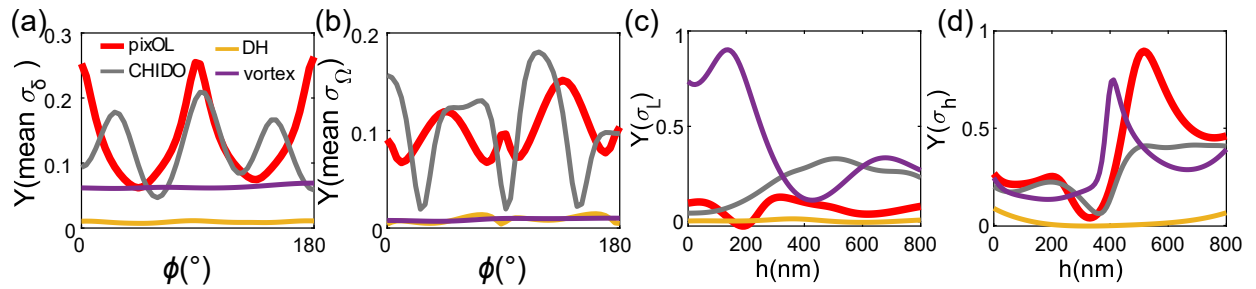
**Fig. S12.** Average basis images  $B_a$  (red: x-polarized, blue: y-polarized) used for detecting single molecules (Eqn. S14c). Basis images for an emitter at  $h = 0$  nm and  $h = 900$  nm are averaged together. The image intensities are normalized relative to the brightest basis image ( $B_{xx}$ ). Colorbars: normalized intensity. Scalebar: 500 nm.



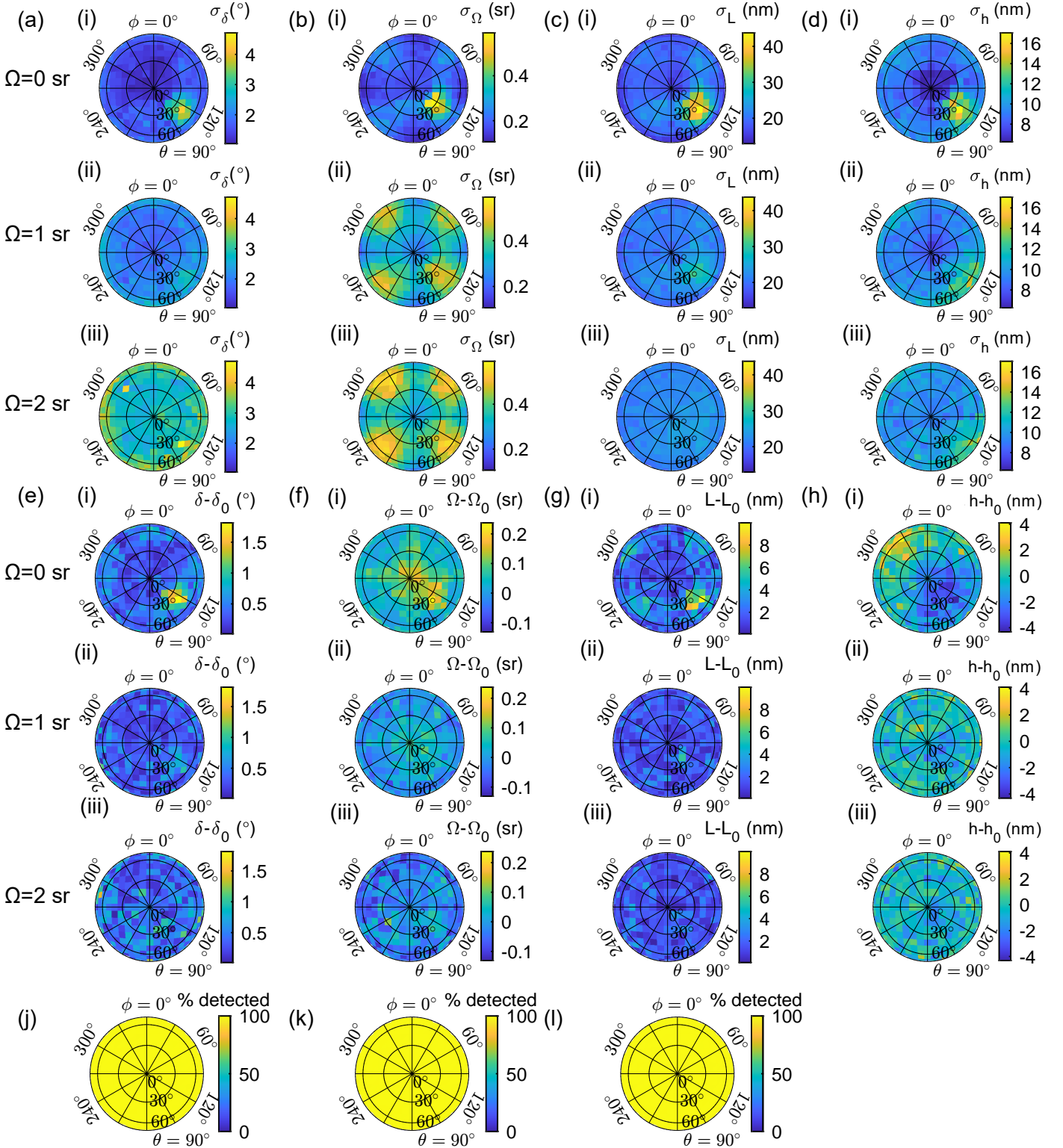
**Fig. S13.** Single-molecule detection and position estimation using the pixOL microscope. (a-d) Polarization-resolved images (red: x and blue: y) of Nile red within spherical lipid bilayers (DPPC with cholesterol). The lateral position  $[x, y]$  of each detected molecule is overlaid as crosses (blue cross in the x-polarized image and red cross in the y-polarized image). Scale bar: 500 nm. Color bar: photons/pixel.



**Fig. S14.** Coupling between different position and orientation parameters for pixOL compared to other methods. (a-d) Average of the entries in the Fisher information matrix  $\mathbf{K}^{-1}$  for estimating 3D orientation, rotational wobble, and 3D position when using (a) pixOL, (b) CHIDO [13], (c) double helix [14], and (d) unpolarized vortex [15]. Averages are computed over all orientations and for emitters located within an axial range of  $h \in [0, 800]$ . To normalize the matrix, element  $\mathbf{K}_{[i,j]}^{-1}$  in  $i^{\text{th}}$  row and  $j^{\text{th}}$  column is divided by  $\mathbf{K}_{[i,i]}^{-1/2} \mathbf{K}_{[j,j]}^{-1/2}$ . The emitters are immersed in water (1.33 refractive index) and imaged using an objective focused at a normal focal plane of  $-580$  nm, collecting 2500 signal photons and 3 background photons per pixel.

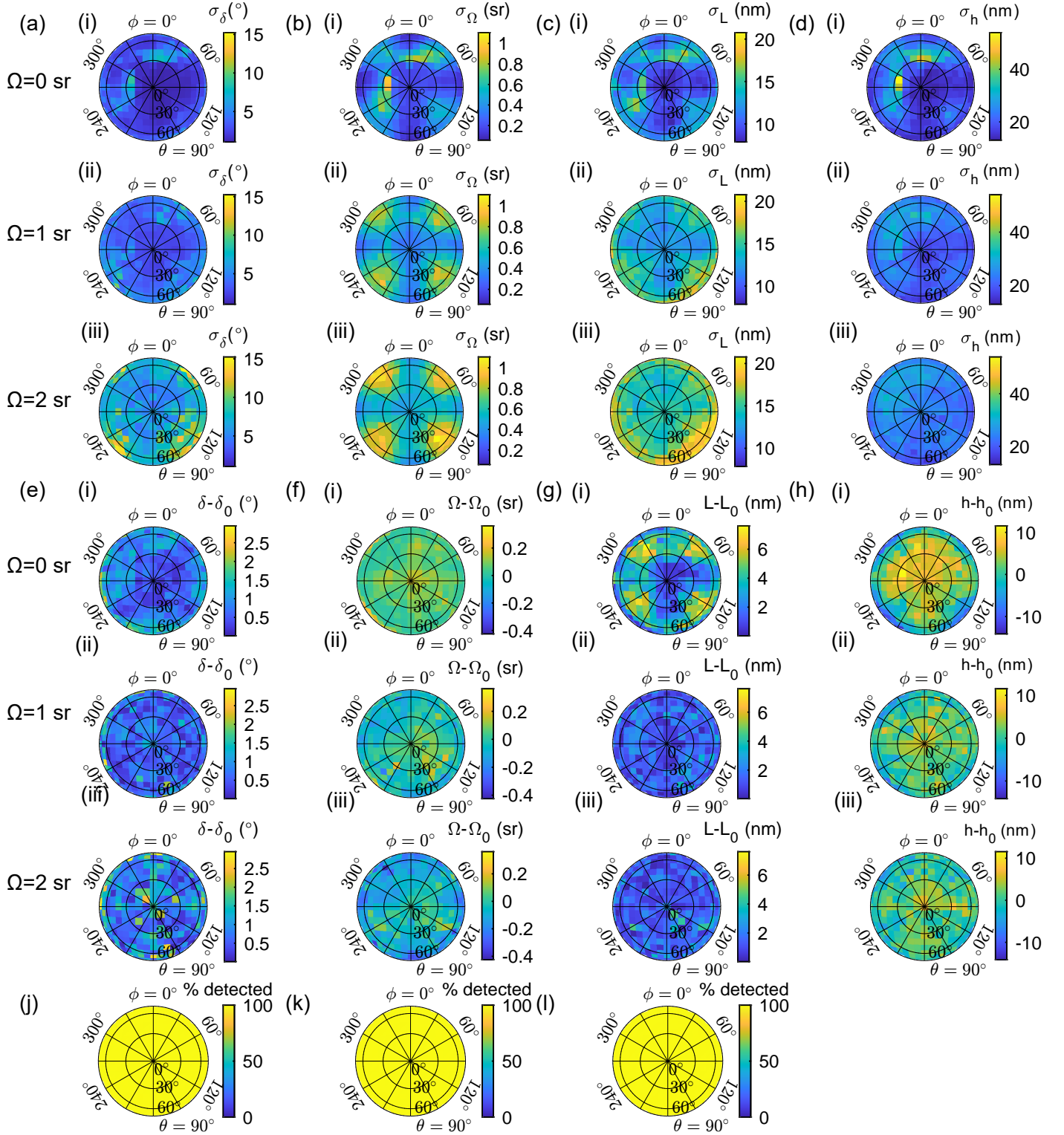


**Fig. S15.** Influence of 3D orientation-3D position correlations on measurement precision. (a) Difference ratio  $Y$ , which quantifies the difference in measurement precision accounting for orientation-position correlations vs. ignoring them (Eqn. S26), for orientation precision  $\sigma_\delta$ , averaged over all polar orientations  $\theta$ . (b) Difference ratio  $Y$  for wobble angle precision  $\sigma_\Omega$ . (c) Difference ratio  $Y$  for lateral localization precision  $\sigma_L$ . (d) Difference ratio  $Y$  for axial localization precision  $\sigma_h$ . In-focus SMs with fixed orientation ( $\Omega = 0$  sr) are used for (a,b); isotropic emitters ( $\Omega = 2\pi$  sr) are used for (c,d). Emitters are immersed in water (1.33 refractive index) with 2500 signal photons and 3 background photons per pixel.

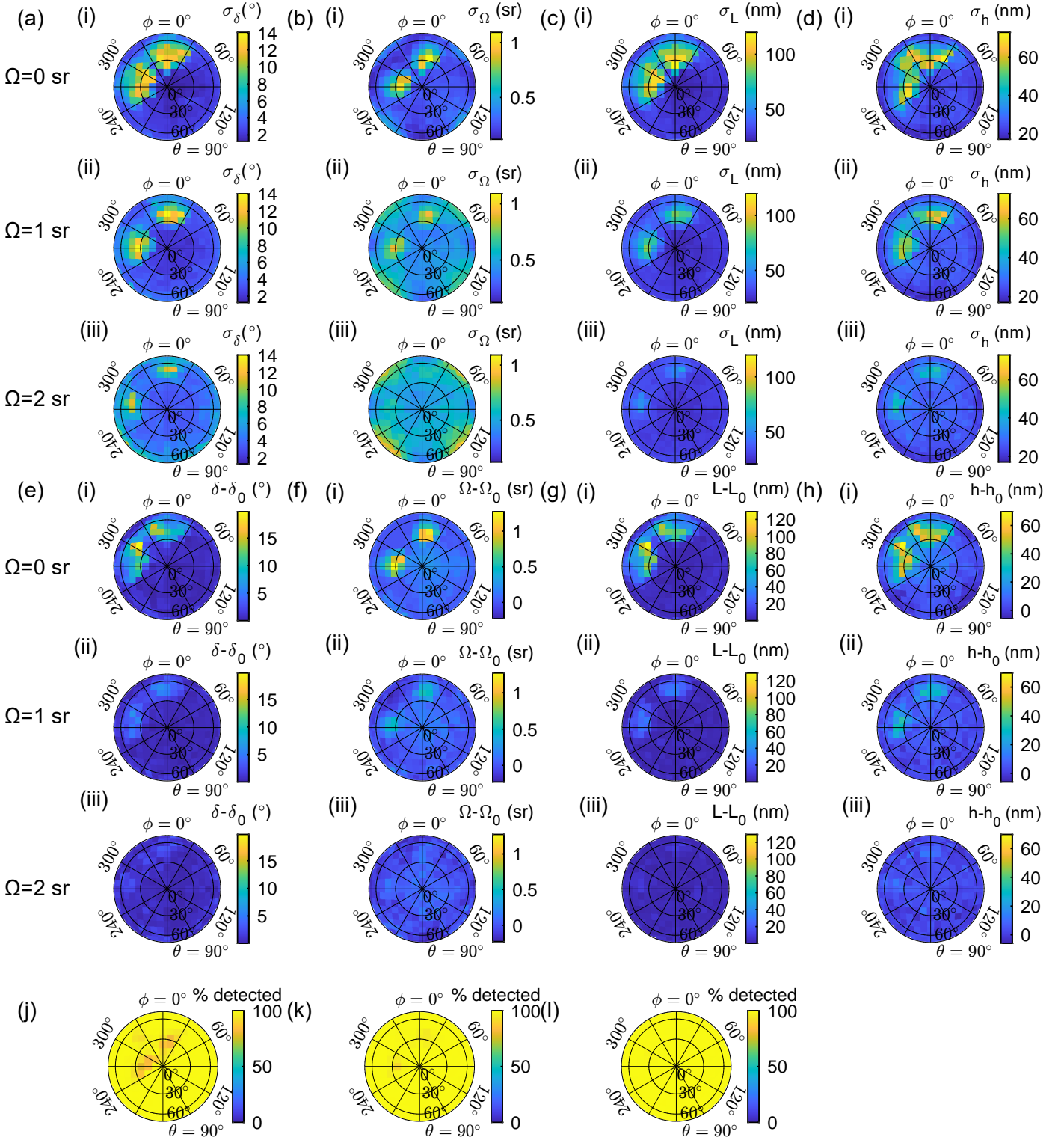


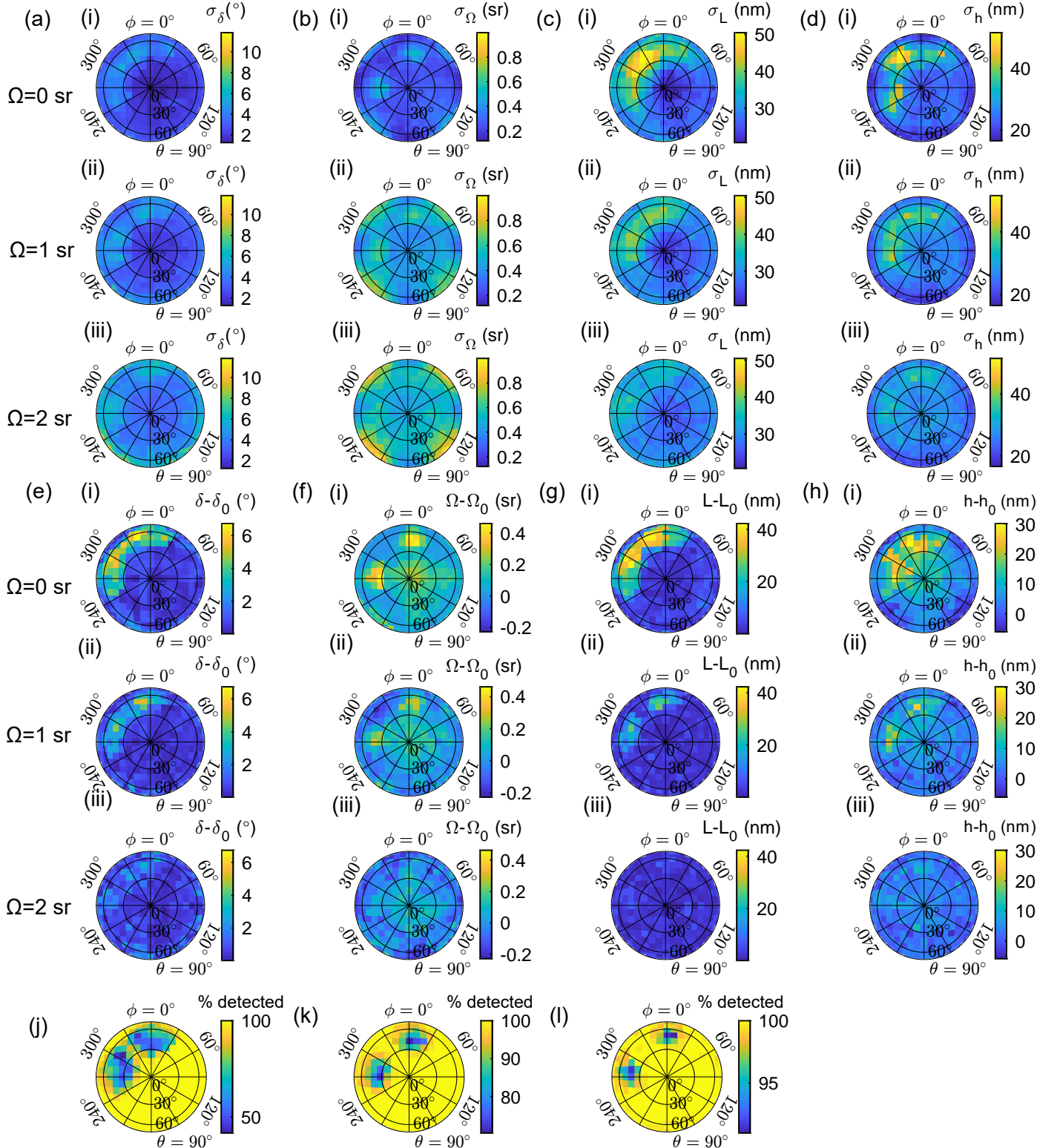
**Fig. S16.** Precision and accuracy of estimating 3D orientation and 3D position for emitters at  $h = 0$  nm with a nominal focal plane placed at  $z = -580$  nm with low background. (a-d) Precision of measuring 3D orientation (a)  $\sigma_\delta$  (deg), (b)  $\sigma_\Omega$  (sr), and 3D location (c)  $\sigma_L$  (nm), (d)  $\sigma_h$  (nm) at various orientations ( $\Omega \in \{0, 1, 2\}$  sr,  $\theta \in [0^\circ, 90^\circ]$ ,  $\phi \in [0^\circ, 360^\circ]$ ). (e-h) Accuracy of measuring 3D position (e)  $\delta - \delta_0$  (deg), (f)  $\Omega - \Omega_0$  (sr), and 3D location (g)  $L - L_0$  (nm), (h)  $h - h_0$  (nm). (j-l) Percentage of trials that successfully detect one emitter for (j)  $\Omega = 0$  sr, (k)  $\Omega = 1$  sr, and (l)  $\Omega = 2$  sr. At each orientation, 200 independent images were generated for emitter within water located at  $h = 0$  nm with 2500 signal photons in total and 3 background photons per pixel detected. The 3D orientation and 3D position are estimated as described in Section 2.



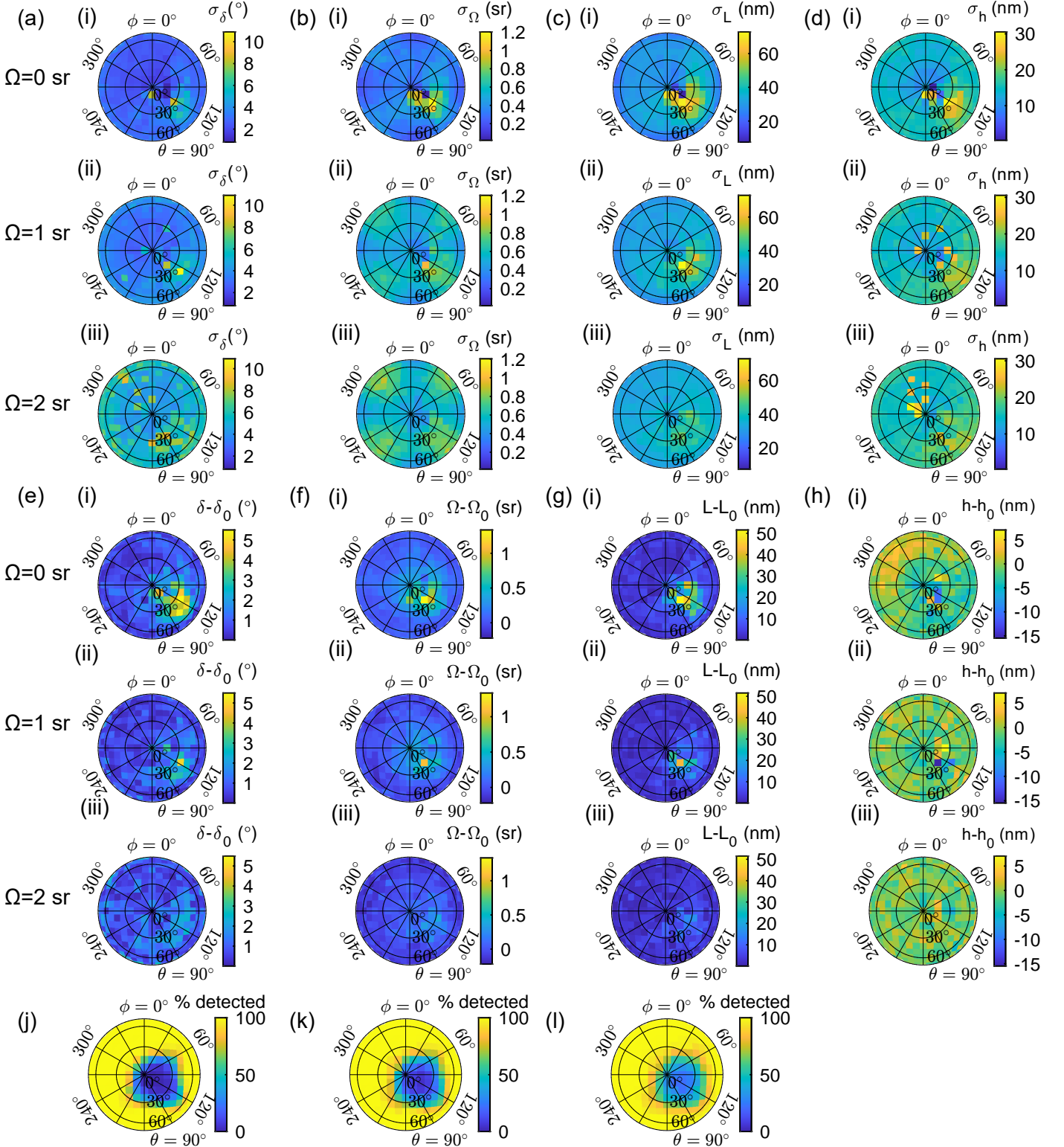


**Fig. S17.** Precision and accuracy of estimating 3D orientation and 3D position for emitters at  $h = 400$  nm with a nominal focal plane placed at  $z = -580$  nm with low background. (a-d) Precision of measuring 3D orientation (a)  $\sigma_\delta$  (deg), (b)  $\sigma_\Omega$  (sr), and 3D location (c)  $\sigma_L$  (nm), (d)  $\sigma_h$  (nm) at various orientations ( $\Omega \in \{0, 1, 2\}$  sr,  $\theta \in [0^\circ, 90^\circ]$ ,  $\phi \in [0^\circ, 360^\circ]$ ). (e-h) Accuracy of measuring 3D orientation (e)  $\delta - \delta_0$  (deg), (f)  $\Omega - \Omega_0$  (sr), and 3D location (g)  $L - L_0$  (nm), (h)  $h - h_0$  (nm). (j-l) Percentage of trials that successfully detect one emitter for (j)  $\Omega = 0$  sr, (k)  $\Omega = 1$  sr, and (l)  $\Omega = 2$  sr. At each orientation, 200 independent images were generated for emitter within water located at  $h = 400$  nm with 2500 signal photons in total and 3 background photons per pixel detected. The 3D orientation and 3D position are estimated as described in Section 2.

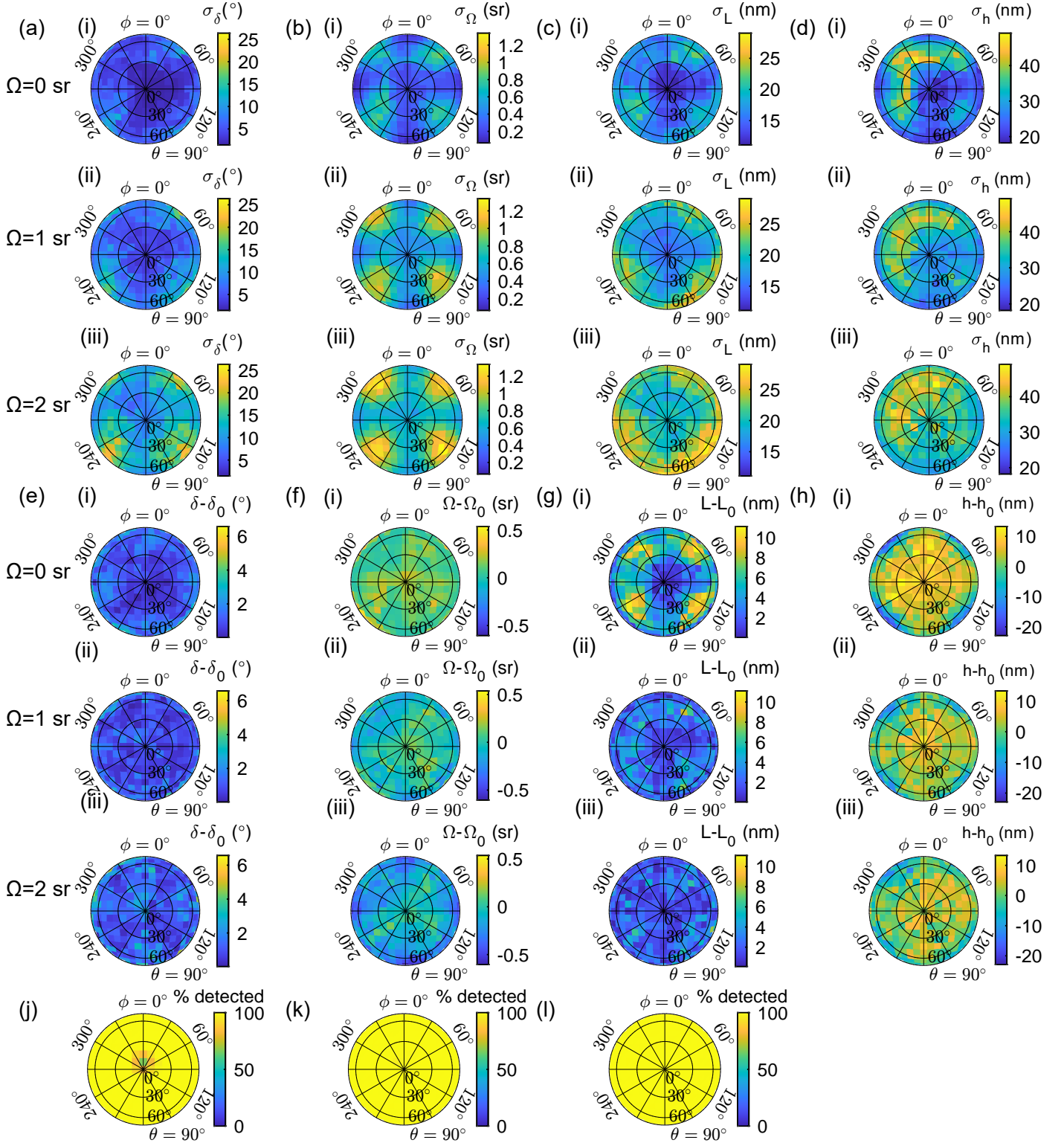




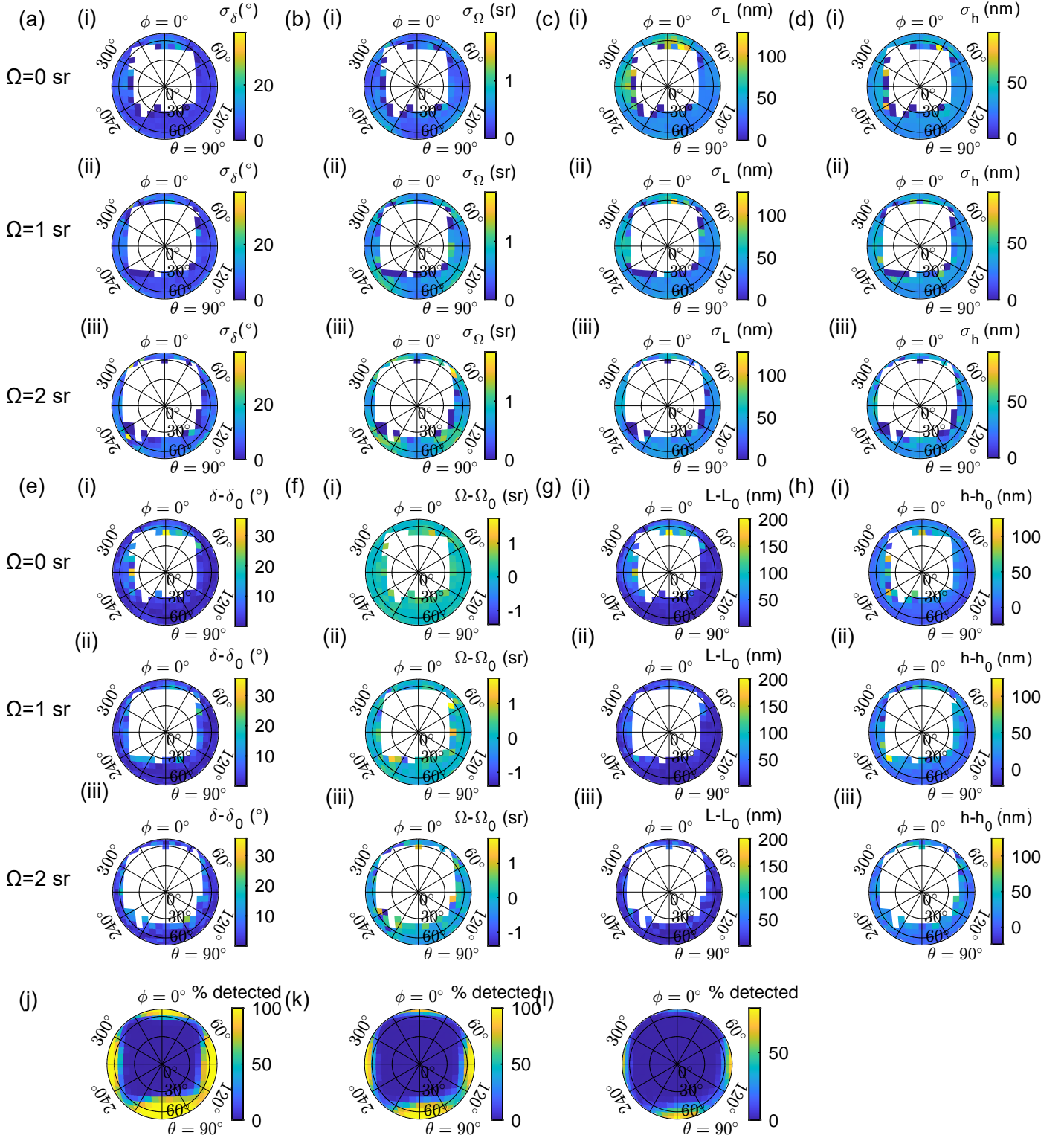
**Fig. S19.** Precision and accuracy of estimating 3D orientation and 3D position for emitters at  $h = 700$  nm with a nominal focal plane placed at  $z = -580$  nm after filtering biased estimates. Estimates  $>90$  nm away from the ground truth 2D position  $(x_0, y_0)$  are removed. (a-d) Precision of measuring 3D orientation (a)  $\sigma_\delta$  (deg), (b)  $\sigma_\Omega$  (sr), and 3D location (c)  $\sigma_L$  (nm), (d)  $\sigma_h$  (nm) at various orientations ( $\Omega \in \{0, 1, 2\}$  sr,  $\theta \in [0^\circ, 90^\circ]$ ,  $\phi \in [0^\circ, 360^\circ]$ ) after filtering. (e-h) Accuracy of measuring 3D orientation (e)  $\delta - \delta_0$  (deg), (f)  $\Omega - \Omega_0$  (sr), and 3D location (g)  $L - L_0$  (nm), (h)  $h - h_0$  (nm). (j-l) Percentage of estimates passing the filter for (j)  $\Omega = 0$  sr, (k)  $\Omega = 1$  sr, and (l)  $\Omega = 2$  sr. At each orientation, 200 independent images were generated for emitter within water located at  $h = 700$  nm with 2500 signal photons and 3 background photons per pixel. The 3D orientation and 3D position are estimated as described in Section 2.



**Fig. S20.** Precision and accuracy of estimating 3D orientation and 3D position for emitters at  $h = 0$  nm with a nominal focal plane placed at  $z = -580$  nm with high background. (a-d) Precision of measuring 3D orientation (a)  $\sigma_\delta$  (deg), (b)  $\sigma_\Omega$  (sr), and 3D location (c)  $\sigma_L$  (nm), (d)  $\sigma_h$  (nm) at various orientations ( $\Omega \in \{0, 1, 2\}$  sr,  $\theta \in [0^\circ, 90^\circ]$ ,  $\phi \in [0^\circ, 360^\circ]$ ). (e-h) Accuracy of measuring 3D orientation (e)  $\delta - \delta_0$  (deg), (f)  $\Omega - \Omega_0$  (sr), and 3D location (g)  $L - L_0$  (nm), (h)  $h - h_0$  (nm). (j-l) Percentage of trials that successfully detect one emitter for (j)  $\Omega = 0$  sr, (k)  $\Omega = 1$  sr, and (l)  $\Omega = 2$  sr. At each orientation, 200 independent images were generated for emitter within water located at  $h = 0$  nm with 2500 signal photons in total and 10 background photons per pixel detected. The 3D orientation and 3D position are estimated as described in Section 2.



**Fig. S21.** Precision and accuracy of estimating 3D orientation and 3D position for emitters at  $h = 400$  nm with a nominal focal plane placed at  $z = -580$  nm with high background. (a-d) Precision of measuring 3D orientation (a)  $\sigma_\delta$  (deg), (b)  $\sigma_\Omega$  (sr), and 3D location (c)  $\sigma_L$  (nm), (d)  $\sigma_h$  (nm) at various orientations ( $\Omega \in \{0, 1, 2\}$  sr,  $\theta \in [0^\circ, 90^\circ]$ ,  $\phi \in [0^\circ, 360^\circ]$ ). (e-h) Accuracy of measuring 3D orientation (e)  $\delta - \delta_0$  (deg), (f)  $\Omega - \Omega_0$  (sr), and 3D location (g)  $L - L_0$  (nm), (h)  $h - h_0$  (nm). (j-l) Percentage of trials that successfully detect one emitter for (j)  $\Omega = 0$  sr, (k)  $\Omega = 1$  sr, and (l)  $\Omega = 2$  sr. At each orientation, 200 independent images were generated for emitter within water located at  $h = 400$  nm with 2500 signal photons in total and 10 background photons per pixel detected. The 3D orientation and 3D position are estimated as described in Section 2.



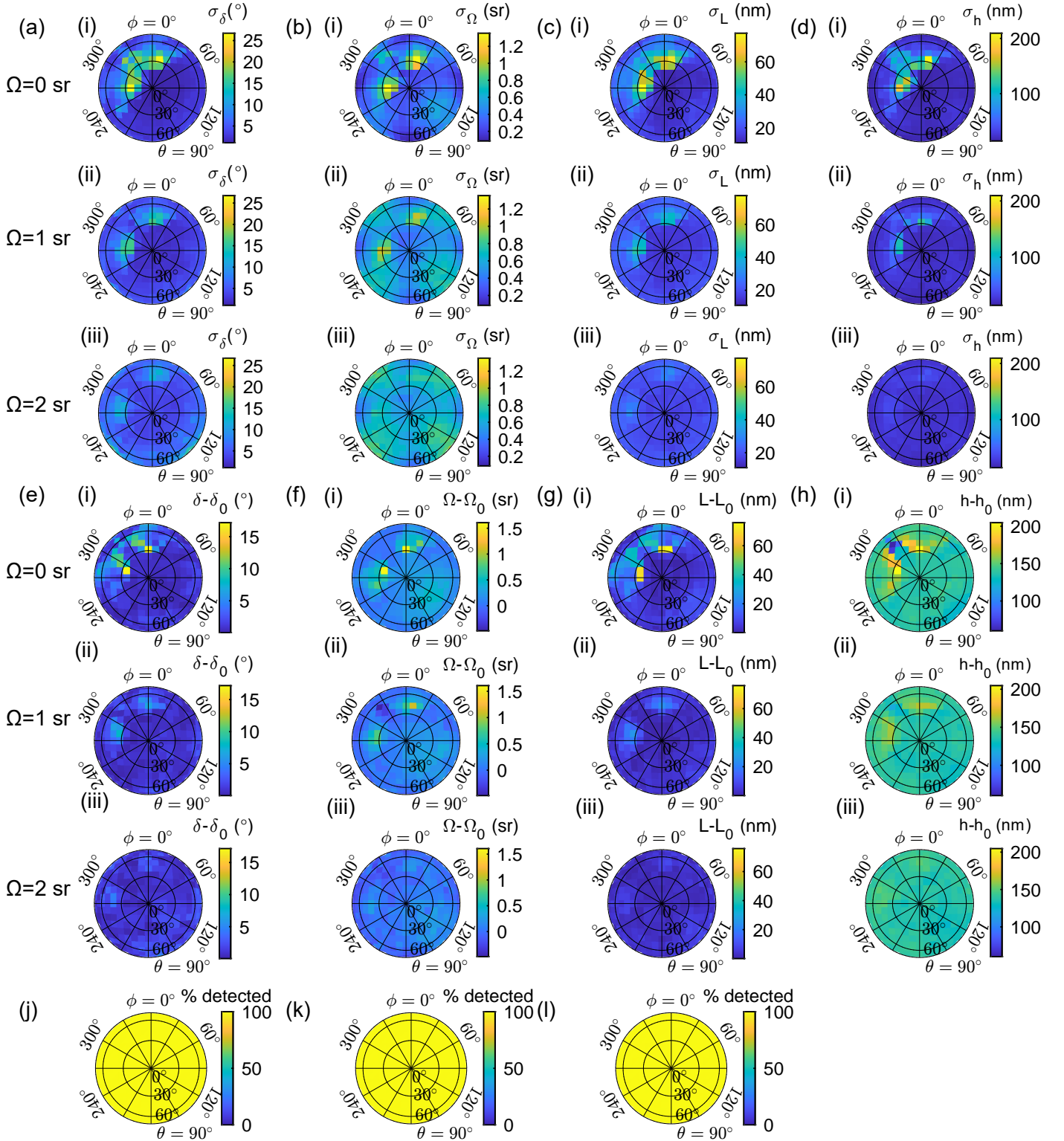


**Fig. S23.** Precision and accuracy of estimating 3D orientation and 3D position for emitters at  $h = 400$  nm with a nominal focal plane placed at  $z = -580$  nm. An incorrect NFP position of  $z = -400$  nm is used for estimation. (a-d) Precision of measuring 3D orientation (a)  $\sigma_\delta$  (deg), (b)  $\sigma_\Omega$  (sr), and 3D location (c)  $\sigma_L$  (nm), (d)  $\sigma_h$  (nm) at various orientations ( $\Omega \in \{0, 1, 2\}$  sr,  $\theta \in [0^\circ, 90^\circ]$ ,  $\phi \in [0^\circ, 360^\circ]$ ). (e-h) Accuracy of measuring 3D orientation (e)  $\delta - \delta_0$  (deg), (f)  $\Omega - \Omega_0$  (sr), and 3D location (g)  $L - L_0$  (nm), (h)  $h - h_0$  (nm). (j-l) Percentage of trials that successfully detect one emitter for (j)  $\Omega = 0$  sr, (k)  $\Omega = 1$  sr, and (l)  $\Omega = 2$  sr. At each orientation, 200 independent images were generated for emitter within water located at  $h = 400$  nm with 2500 signal photons in total and 3 background photons per pixel detected. The 3D orientation and 3D position are estimated as described in Section 2.

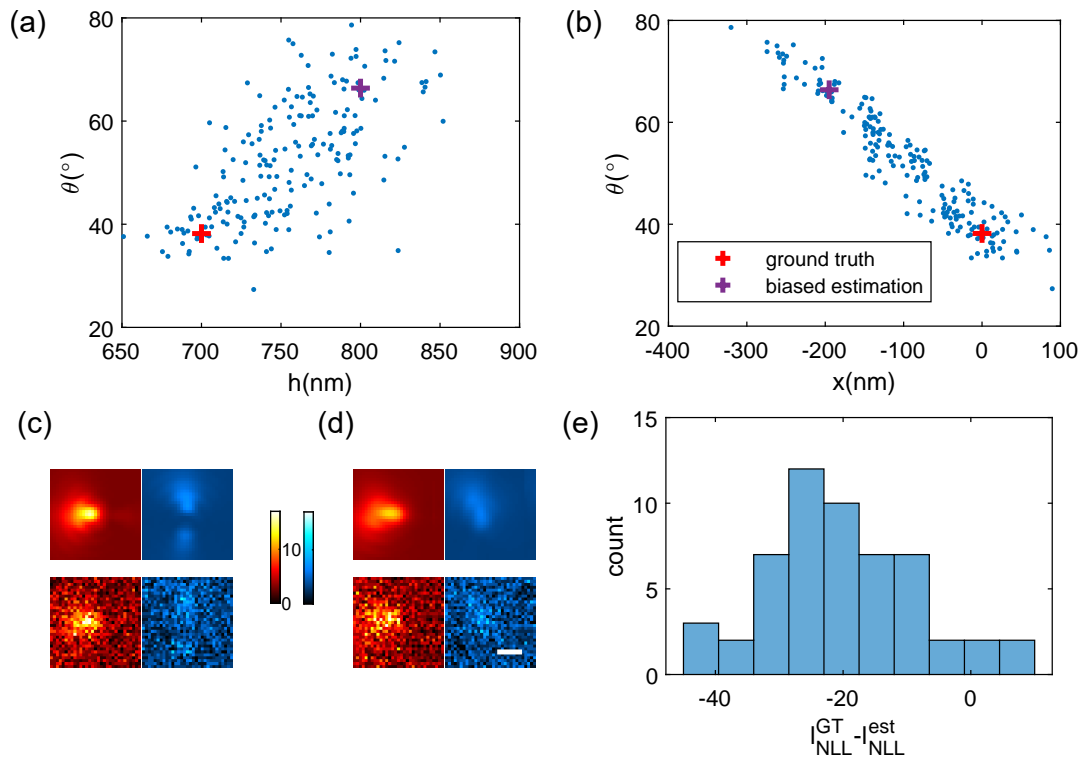


**Fig. S24.** Correlation between measurements of 3D orientation and 3D position for an emitter in water with a nominal focal plane placed at  $z = -580$  nm. The emitter here is located at  $(x_0, y_0, h_0) = (0, 0, 700)$  nm with 3D orientation  $(\theta_0, \phi_0, \Omega_0) = (38^\circ, 162^\circ, 0)$ . The algorithm in Section 2 is used to fit 200 independently generated noisy images. (a) Axial position estimation  $h$  vs. polar angle estimation  $\theta$ . (b) Horizontal position estimation  $x$  vs. polar angle estimation  $\theta$ . (c,d) (top) Noiseless DSF images and (bottom) images with Poisson shot noise for an emitter whose position and orientation match (c) the ground truth and (d) the biased estimate shown in (a,b). (Red) x-polarized, (blue) y-polarized. Colorbar: photons/pixel. Scalebar: 500 nm. (e) Comparing the value of the negative log-likelihood  $l_{\text{NLL}}^{\text{GT}}$  of the ground truth (Eqn. S15) to the value of the negative log likelihood  $l_{\text{NLL}}^{\text{est}}$  of the biased position and orientation ( $>90$  nm away from the ground truth 2D position  $(x_0, y_0)$ ). Negative values indicate that the ground truth position and orientation are more consistent with the noisy image than the biased estimate, i.e.,  $l_{\text{NLL}}^{\text{GT}} < l_{\text{NLL}}^{\text{est}}$ , but our estimation algorithm (Sec. 2) converged to the biased value instead.

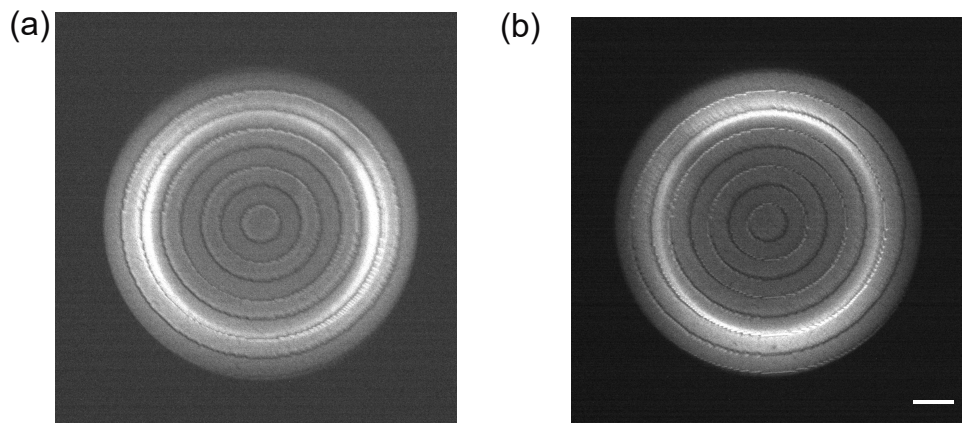


**Fig. S25.** Aligning the spatial light modulator. Back focal plane (BFP) images captured from the (a) x- and (b) y-polarization channels using the flipping mirror in Fig. S1. A binary phase mask consisting of concentric rings of increasing radius (10-pixel interval) is loaded onto the spatial light modulator (SLM). The center of the phase mask is calibrated by matching the center of ring pattern to the center of the objective lens pupil. Obtaining sharp images of the ring pattern and pupil simultaneously ensures that the phase mask is positioned properly along the optical axis. The BFPs shown here are illuminated by a single layer of fluorescent spheres on coverglass exposed to air. Scale bar: 500  $\mu\text{m}$ .



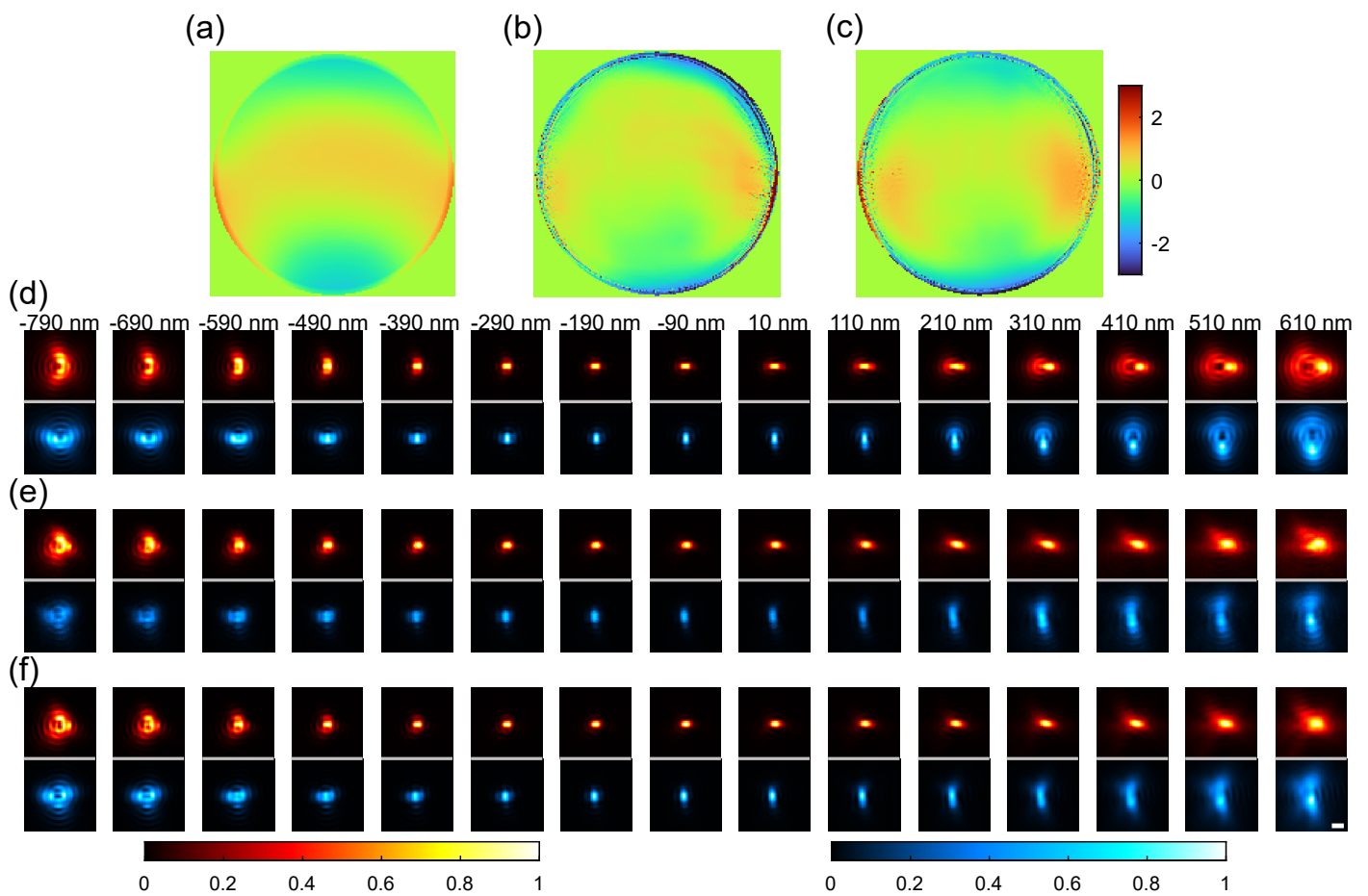


**Fig. S26.** Calibration of the pixOL phase mask. (a) Perfect pixOL phase mask. (b,c) Calibrated experimental pupil phase patterns from the (b) x and (c) y polarization channels. Colorbar: phase (rad). (d) Ideal pixOL DSFs (red: x-polarized, blue: y-polarized) for various defocus positions  $z = -790$  nm to  $z = 610$  nm. (e) Experimental DSFs. (f) Simulated DSFs using the calibrated phase masks in (b) and (c). The intensities of each red-blue image pair are normalized. Colorbar: normalized intensity. Scalebar: 400 nm.

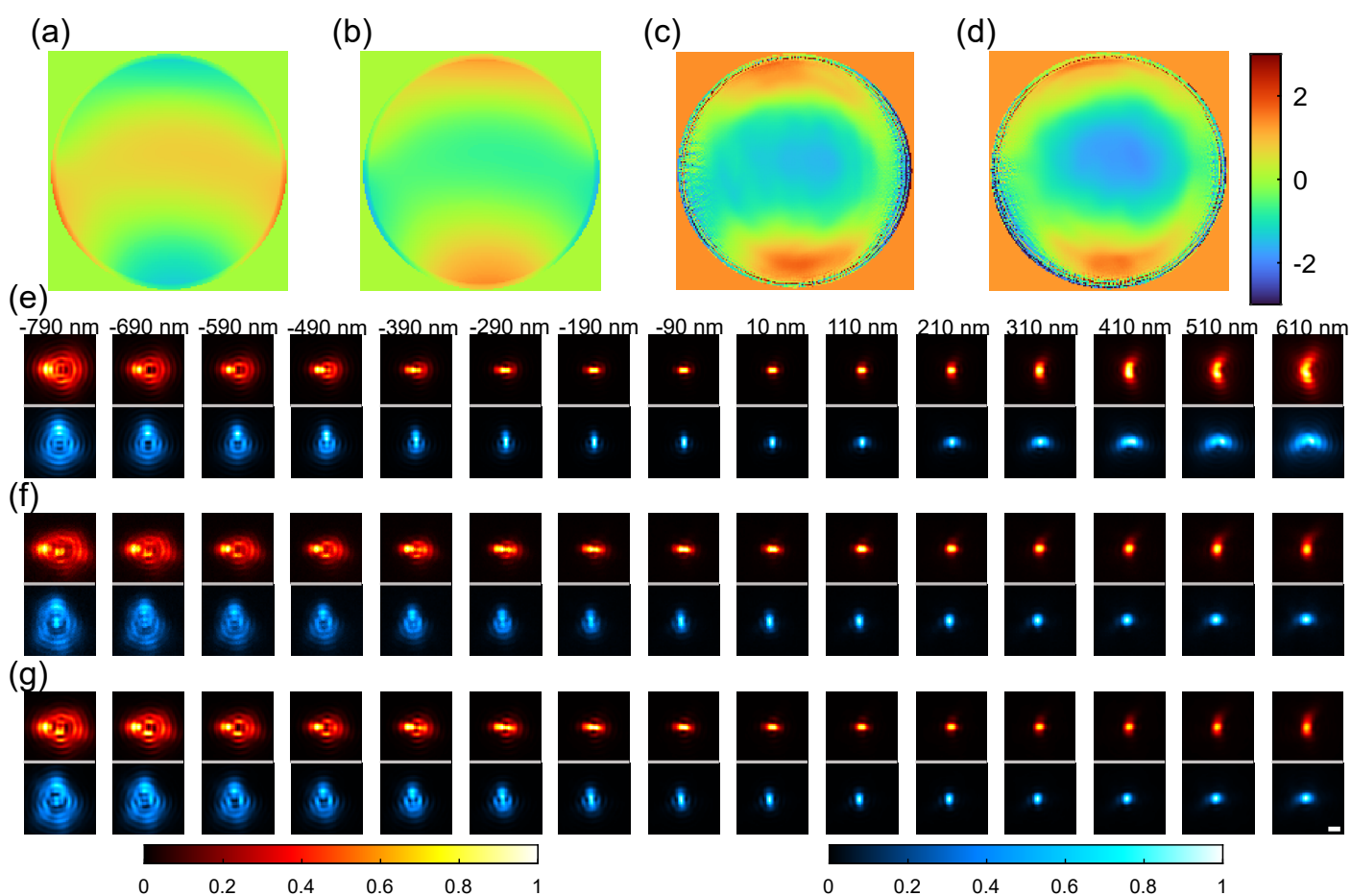


**Fig. S27.** Calibration of the conjugate pixOL phase mask (pixOL\*). (a) Perfect pixOL phase mask. (b) Perfect pixOL\* phase mask. (c,d) Calibrated experimental pupil phase patterns from the (c) x and (d) y polarization channels. Colorbar: phase (rad). (e) Ideal pixOL\* DSFs (red: x-polarized, blue: y-polarized) for various defocus positions  $z = -790$  nm to  $z = 610$  nm. (f) Experimental DSFs. (g) Simulated DSFs using the calibrated phase masks in (c) and (d). The intensities of each red-blue image pair are normalized. Colorbar: normalized intensity. Scalebar: 400 nm.

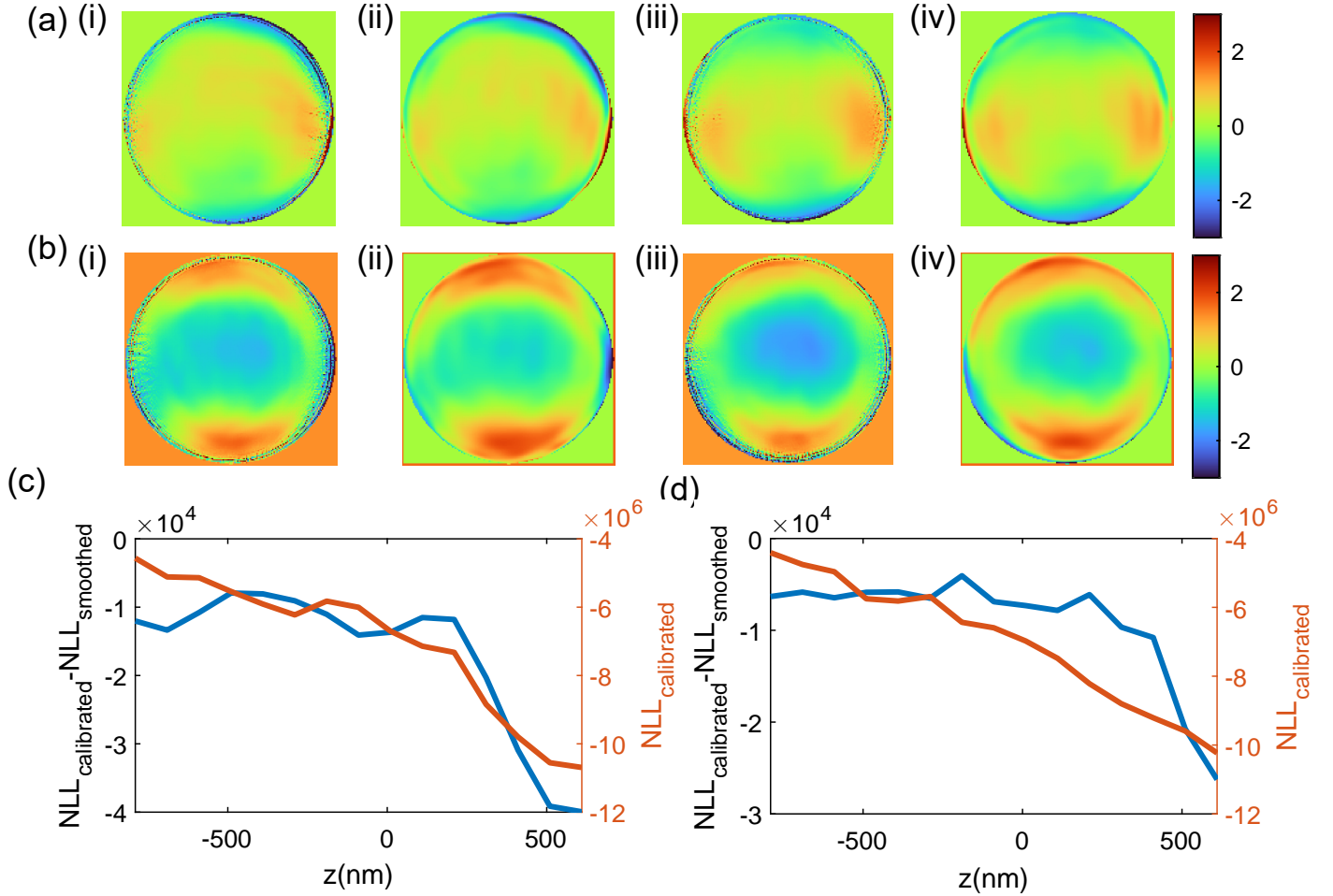


**Fig. S28.** Comparison between calibrated phase masks and their smoothed versions for pixOL and pixOL\*. (a,b) The calibrated (a) pixOL (b) pixOL\* phase masks from the (i) x and (iii) y polarization channels. Smoothed versions of the (a) pixOL and (b) pixOL\* phase mask are shown corresponding to DSFs in the (ii) x and (iv) y polarization channels. The smoothed phase masks are reconstructed by projecting the calibrated phase masks into a Zernike basis using the first 231 Zernike polynomials. Colorbar: phase (rad). (c,d) Comparing model accuracy using the negative log likelihood (NLL, Eqn. S15) between simulated dipole spread functions (DSFs) and images of fluorescent beads in Figs. S26(d) and S27(e) across all axial positions  $z$ . Differences in NLL are calculated for DSFs using the calibrated ( $NLL_{\text{calibrated}}$ ) vs. smoothed phase masks ( $NLL_{\text{smoothed}}$ ) for (c) pixOL and (d) pixOL\*. Blue:  $NLL_{\text{calibrated}} - NLL_{\text{smoothed}}$ ; orange:  $NLL_{\text{calibrated}}$ .

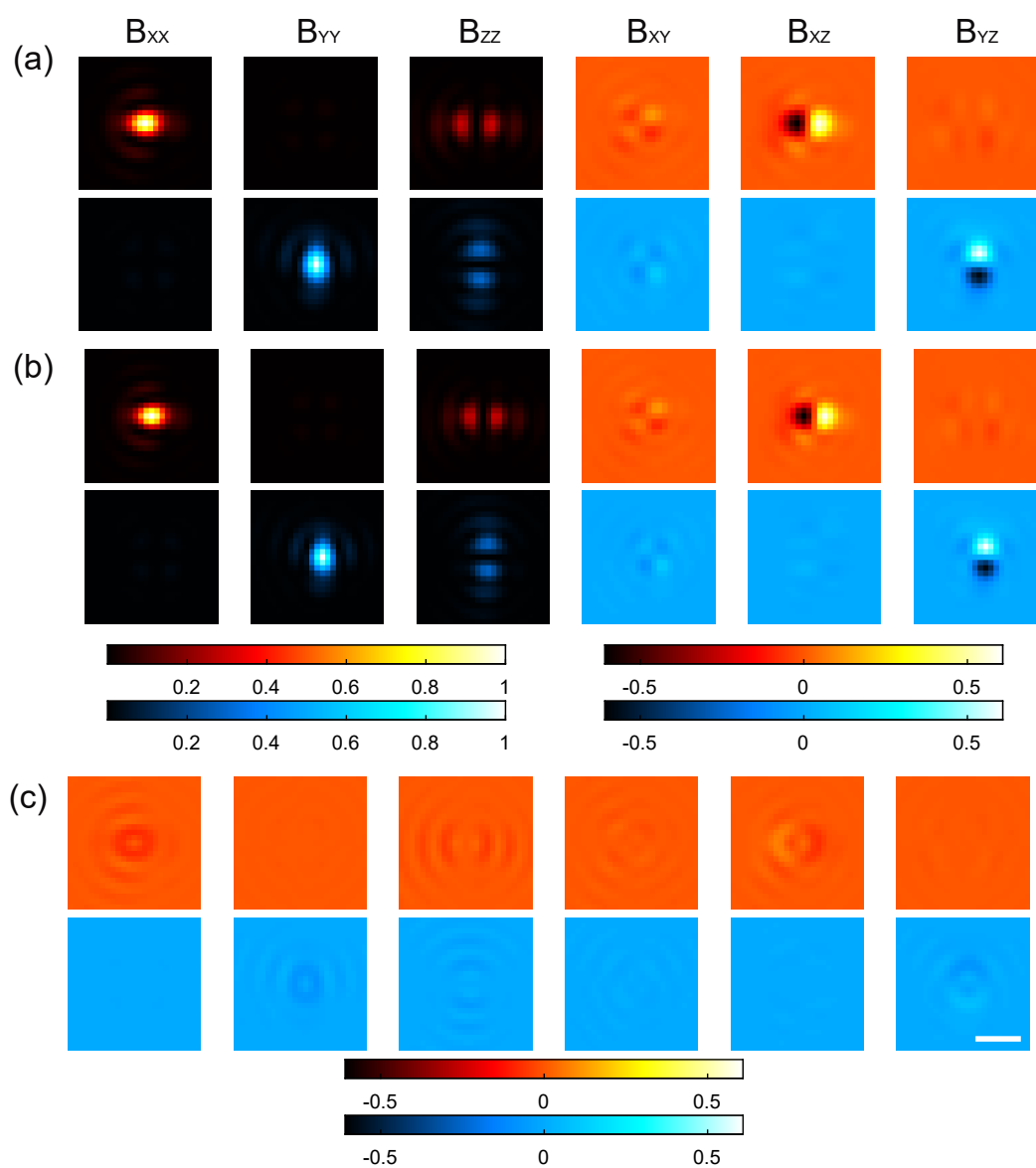


**Fig. S29.** Image-plane basis images  $\mathbf{B}$  of the pixOL phase mask shown in Fig. 1(a,c) for an in-focus emitter of wavelength (a) 641 nm and (b) 582 nm. The image intensities for each wavelength are normalized relative to the brightest basis image ( $B_{xx}$ ). (c) The difference between basis images in (a) and (b). Colorbars: normalized intensity. Scalebar: 500 nm.

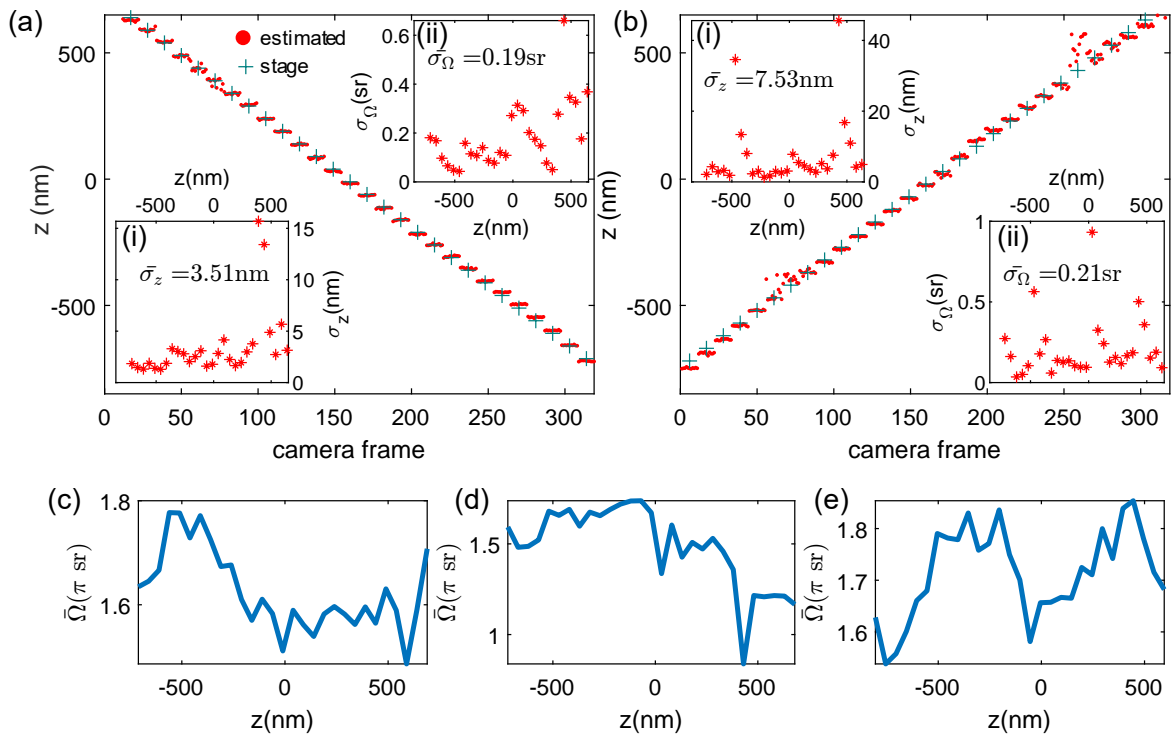


**Fig. S30.** Position and emission anisotropy measurements of two fluorescent beads. (a) Trajectory of defocus estimates  $z$  for a bead scanned axially from  $z = -790$  nm to  $z = 610$  nm with a step size of 50 nm (11 camera frames per step). (b) Same as (a), but for another bead scanned in the opposite direction. Red dot: estimated axial distance  $z$  between the bead and focal plane in each frame; green cross: expected stage position. Inset (i): Experimental axial precision  $\sigma_z$  at each scanning plane (mean precision  $\bar{\sigma}_z$  is (a) 3.51 nm and (b) 7.53 nm). Inset (ii): Experimental emission anisotropy precision  $\sigma_\Omega$  at each scanning plane (average precision  $\bar{\sigma}_\Omega$  is (a) 0.19 sr and (b) 0.21 sr). (c-e) Mean emission anisotropies of 3 fluorescent beads quantified as an effective wobble angle  $\bar{\Omega}$  at each scanning plane: (c) bead in (a), (d) bead in (b), and (e) bead in Fig. 2(e).

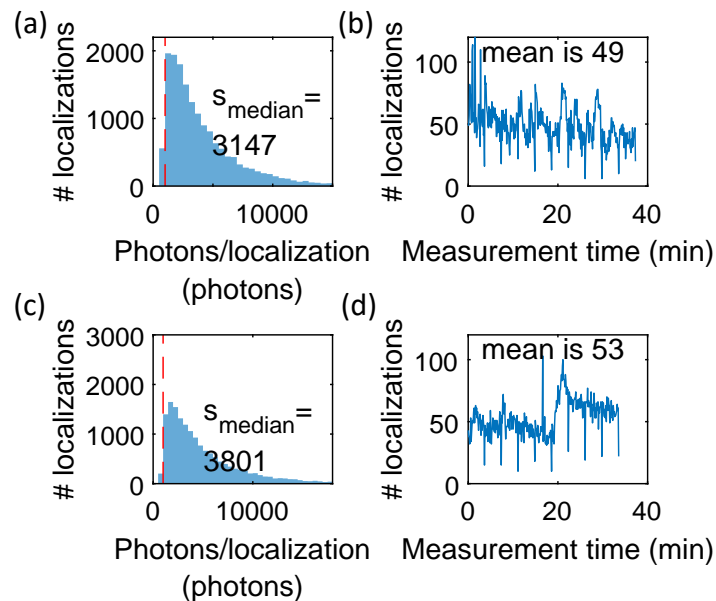


**Fig. S31.** Photophysics of Nile red (NR) blinking events. (a,c) Photons  $s$  detected per localization of Nile red within spherical supported lipid bilayers (SLBs) consisting of (a) DPPC plus cholesterol and (c) DPPC only. The red dashed line represents  $s = 1000$  photons. (b,d) Localization rate per 0.11 minutes for NR within (b) DPPC plus cholesterol and (d) DPPC-only SLBs.

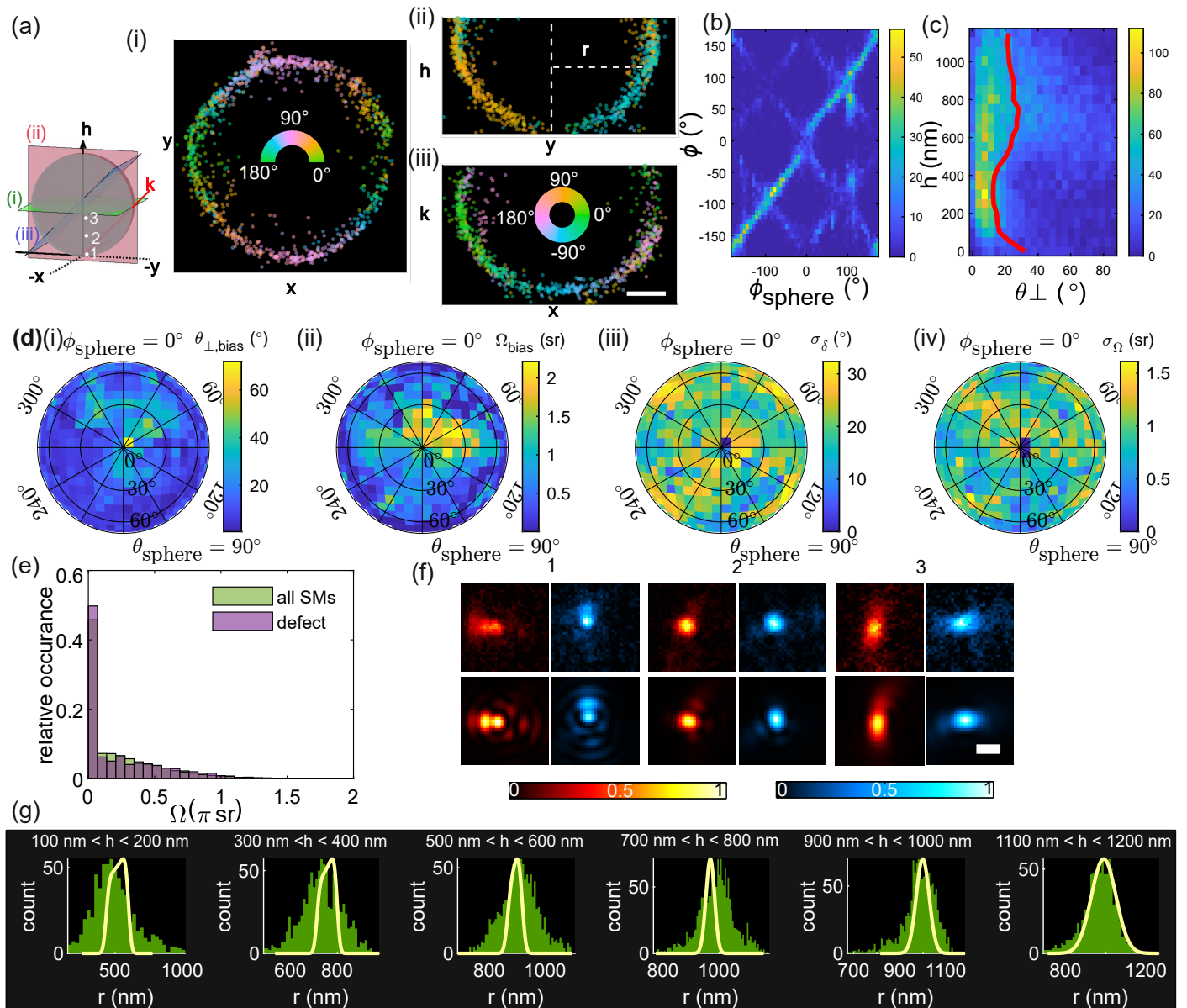


**Fig. S32.** SMOLM images of the 3D orientations and 3D locations of Nile red (NR) within a spherical supported lipid bilayer consisting of DPPC plus cholesterol. (a) Azimuthal angle  $\phi$  of each NR molecule for the three cross-sections in inset: (i) x-y slice, (ii) y-h slice, and (iii) plane with  $y+h=1000$  nm. Each slice has a thickness of 100 nm. Colorbar:  $\phi$  (deg). (ii) and (iii) shares the same colormap shown in (iii). Scalebar: 400 nm. (b) NR orientations  $\phi$  relative to their positions on the sphere's surface  $\phi_{\text{sphere}}$ . (c) NR axial locations  $h$  vs. orientations  $\theta_{\perp}$ . Colorbars: SM counts per bin. Red line: median value of  $\theta_{\perp}$  at each axial location  $h$ . (d) Experimental estimated bias in measuring NR (i) orientation  $\theta_{\perp,\text{bias}}$  and (ii) wobble angle  $\Omega_{\text{bias}}$ , plotted as a function of NR position on the spherical surface  $[\theta_{\text{sphere}}, \phi_{\text{sphere}}]$  of the SLB, assuming that the ground truth orientations of NR are normal to the spherical surface ( $\theta_{\perp} = 0$ ) and completely fixed ( $\Omega = 0$  sr). (iii,iv) Same as (i,ii) but for (iii) angular standard deviation  $\sigma_{\delta}$  (Eqn. S23) and (iv) wobble angle precision  $\sigma_{\Omega}$ . (e) NR wobble  $\Omega$  for (green) all localizations over the sphere and (purple) molecules within the membrane defect in Fig. 3(e). (f, top row) Sum of all pixOL images of NR located within a  $50 \times 50 \times 100$  nm<sup>3</sup> box at three locations in (a) inset: (1)  $h = 150$  nm, (2)  $h = 550$  nm, (3)  $h = 950$  nm. (f, bottom row) Simulated pixOL images for emitters oriented perpendicular to the SLB and centered at the three dots locations in (a) inset with  $\phi_{\text{sphere}} = 135^{\circ}$ . (Red) x-polarized, (blue) y-polarized. Colorbars: normalized intensity. Scalebar: 500 nm. (g) NR lateral positions  $r$  (see (a)(ii)) relative to the sphere's center within each  $h$  slice compared to a model distribution (yellow lines, Eqn. S27), accounting for the curved spherical surface and pixOL's localization precision.

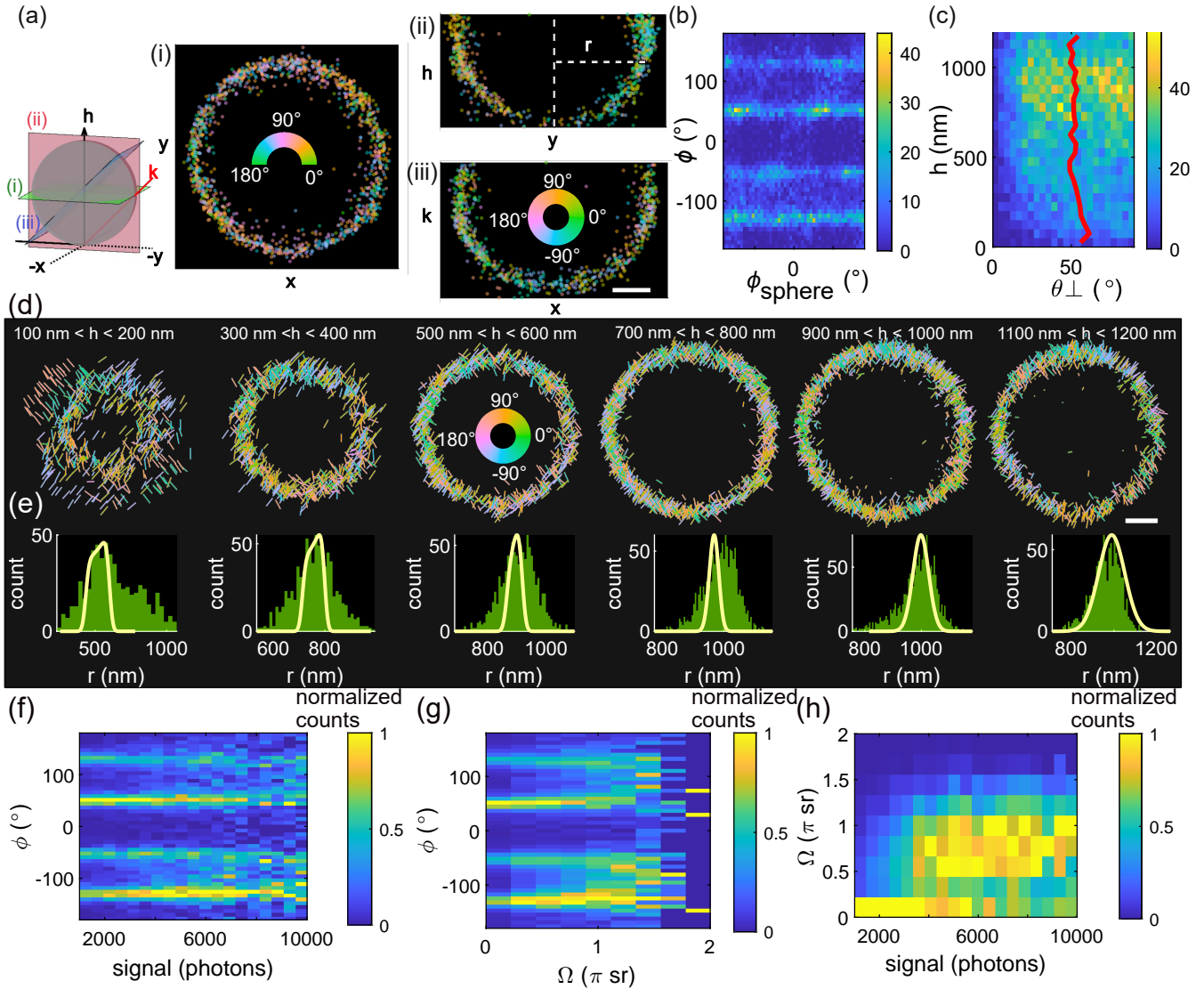


**Fig. S33.** SMOLM images of the 3D orientations and 3D locations of Nile red (NR) within a spherical supported lipid bilayer consisting of DPPC only. (a) Azimuthal angle  $\phi$  of each NR molecule for three slices in inset: (i) x-y slice, (ii) y-h slice, and (iii) plane with  $y+h=1000$  nm. Each slice has a thickness of 100 nm. Colorbar:  $\phi$  (deg). (ii) and (iii) shares the same colormap shown in (iii). (b) NR orientations  $\phi$  relative to their positions on the sphere's surface  $\phi_{\text{sphere}}$  for estimations with signal photons larger than 1000. (c) NR axial locations  $h$  vs. orientations  $\theta_{\perp}$  for estimations with signal photons larger than 1000. Colorbars: SM counts per bin. Red line: the median value of  $\theta_{\perp}$  at each axial location  $h$ . (d) x-y cross-sections of the bead depicting the 3D orientation ( $\theta, \phi$ ) of each NR as a line segment. The length and direction of each line indicate in-plane magnitude  $(\mu_x^2 + \mu_y^2)^{1/2}$  and azimuthal orientation  $\phi$ , respectively. Colors represent azimuthal orientation  $\phi$ . (e) NR lateral positions  $r$  (see (a)(ii)) relative to the sphere's center within each  $h$  slice compared to a model distribution (yellow lines, Eqn. S27), accounting for the curved spherical surface and pixOL's localization precision. (f,g) NR azimuthal orientations  $\phi$  relative to their (f) signal photons and (g) wobble angles  $\Omega$ . (h) NR wobble angle  $\Omega$  relative to their signal photons. For clarity, each column in (f-h) is normalized independently. Scalebars: 400 nm.

Movie S1 Demonstration of SM detection and position-orientation estimation using the pixOL microscope. (Top) Polarized images (red: x-polarized and blue: y-polarized) of Nile red are compared to (bottom) reconstructed images of the pixOL DSF using 3D orientations and 3D positions estimated by the algorithm described in Section 2. Individual Nile red molecules are shown binding transiently to lipids (DPPC with cholesterol) within a spherical bilayer (Figs. 3 and S32). Colorbar: photons/pixel. Scale bar: 1  $\mu\text{m}$ .

Movie S2 3D view of 6D SMOLM imaging of Nile red within spherical supported lipid bilayers consisting of (top) DPPC plus cholesterol (chol, Figs. 3 and S32) and (bottom) DPPC-only (Fig. S33). The position and orientation of each line depicts an emitter's 3D position and 3D orientation. Colors represent polar orientation  $\theta$ .

Movie S3 x-y cross-sections of 6D SMOLM imaging of Nile red within spherical supported lipid bilayers consisting of (top) DPPC plus cholesterol (chol, Figs. 3 and S32) and (bottom) DPPC only (Fig. S33) at various h-slices. The position and orientation of each line depicts an emitter's lateral position and 3D orientation. Colors represent azimuthal orientation  $\phi$ .

13. V. Curcio, L. A. Alemán-Castañeda, T. G. Brown, S. Brasselet, and M. A. Alonso, "Birefringent Fourier filtering for single molecule coordinate and height super-resolution imaging with dithering and orientation," *Nat. Commun.* **11**, 5307 (2020).
14. M. P. Backlund, M. D. Lew, A. S. Backer, S. J. Sahl, G. Grover, A. Agrawal, R. Piestun, and W. E. Moerner, "Simultaneous, accurate measurement of the 3D position and orientation of single molecules," *Proc. Natl. Acad. Sci.* **109**, 19087–19092 (2012).
15. C. N. Hulleman, R. Ø. Thorsen, E. Kim, C. Dekker, S. Stallinga, and B. Rieger, "Simultaneous orientation and 3D localization microscopy with a Vortex point spread function," *Nat. Commun.* **12**, 5934 (2021).
16. O. Zhang and M. D. Lew, "Quantum limits for precisely estimating the orientation and wobble of dipole emitters," *Phys. review research* **2**, 33114 (2020).
17. O. Zhang and M. D. Lew, "Single-molecule orientation localization microscopy II: a performance comparison," *J. Opt. Soc. Am. A* **38**, 288 (2021).
18. O. Zhang, J. Lu, T. Ding, and M. D. Lew, "Imaging the three-dimensional orientation and rotational mobility of fluorescent emitters using the Tri-spot point spread function," *Appl. Phys. Lett.* **113**, 031103 (2018).

## REFERENCES

1. A. S. Backer and W. E. Moerner, "Extending Single-Molecule Microscopy Using Optical Fourier Processing," *The J. Phys. Chem. B* **118**, 8313–8329 (2014).
2. T. Ding, T. Wu, H. Mazidi, O. Zhang, and M. Lew, "Single-molecule orientation localization microscopy for resolving structural heterogeneities within amyloid fibrils," *Optica* **7**, 602–607 (2020).
3. M. Böhmer and J. Enderlein, "Orientation imaging of single molecules by wide-field epifluorescence microscopy," *J. Opt. Soc. Am. B* **20**, 554 (2003).
4. T. Chandler, H. Shroff, R. Oldenbourg, and P. La Rivière, "Spatio-angular fluorescence microscopy II. Paraxial  $4f$  imaging," *J. Opt. Soc. Am. A* **36**, 1346–1360 (2019).
5. O. Zhang and M. D. Lew, "Single-molecule orientation localization microscopy I: fundamental limits," *J. Opt. Soc. Am. A* **38**, 277 (2021).
6. G. Marsaglia, "Choosing a Point from the Surface of a Sphere," *The Annals Math. Stat.* **43**, 645–646 (1972).
7. H. Mazidi, E. S. King, O. Zhang, A. Nehorai, and M. D. Lew, "Dense Super-Resolution Imaging of Molecular Orientation Via Joint Sparse Basis Deconvolution and Spatial Pooling," in *2019 IEEE 16th International Symposium on Biomedical Imaging (ISBI 2019)*, vol. 2019-April (IEEE, 2019), pp. 325–329.
8. A. Beck and M. Teboulle, "A Fast Iterative Shrinkage-Thresholding Algorithm for Linear Inverse Problems," *SIAM J. on Imaging Sci.* **2**, 183–202 (2009).
9. H. Mazidi, J. Lu, A. Nehorai, and M. D. Lew, "Minimizing Structural Bias in Single-Molecule Super-Resolution Microscopy," *Sci. Reports* **8**, 13133 (2018).
10. T. Chandler, S. Mehta, H. Shroff, R. Oldenbourg, and P. J. La Rivière, "Single-fluorophore orientation determination with multiview polarized illumination: modeling and microscope design," *Opt. Express* **25**, 31309 (2017).
11. J. Lu, H. Mazidi, T. Ding, O. Zhang, and M. D. Lew, "Single-Molecule 3D Orientation Imaging Reveals Nanoscale Compositional Heterogeneity in Lipid Membranes," *Angewandte Chemie - Int. Ed.* **59**, 17572–17579 (2020).
12. B. Ferdman, E. Nehme, L. E. Weiss, R. Orange, O. Alalouf, and Y. Shechtman, "VIPR: vectorial implementation of phase retrieval for fast and accurate microscopic pixel-wise pupil estimation," *Opt. Express* **28**, 10179 (2020).